# Novel phases in a square-lattice frustrated ferromagnet :
# $\frac{1}{3}$-magnetization plateau, helicoidal spin liquid, and vortex crystal

Luis Seabra,[1,2] Philippe Sindzingre,[3] Tsutomu Momoi,[4,5] and Nic Shannon[2,6]

[1]*Department of Physics, Technion-Israel Institute of Technology, Haifa 32000, Israel*
[2]*H. H. Wills Physics Laboratory, University of Bristol, Tyndall Avenue, Bristol BS8 1TL, United Kingdom*
[3]*Laboratoire de Physique Théorique de la Matière Condensée, UMR 7600, CNRS, UPMC Université Paris 06,*
*Sorbonne Universités, case 121, 4 Place Jussieu, FR-75252 Paris Cedex, France*
[4]*Condensed Matter Theory Laboratory, RIKEN, Wako, Saitama 351-0198, Japan*
[5]*RIKEN Center for Emergent Matter Science (CEMS), Wako, Saitama 351-0198, Japan*
[6]*Okinawa Institute for Science and Technology Graduate University, Onna-son, Okinawa 904-0495, Japan*

A large part of the interest in magnets with frustrated antiferromagnetic interactions comes from the many new phases found in applied magnetic field. In this article, we explore some of the new phases which arise in a model with frustrated *ferromagnetic* interactions, the $J_1$-$J_2$-$J_3$ Heisenberg model on a square lattice. Using a combination of classical Monte Carlo simulation and spin-wave theory, we uncover behavior reminiscent of some widely studied frustrated antiferromagnets, but with a number of new twists. We first demonstrate that, for a suitable choice of parameters, the phase diagram as a function of magnetic field and temperature is nearly identical to that of the Heisenberg antiferromagnet on a triangular lattice, including the celebrated 1/3-magnetization plateau. We then examine how this phase diagram changes when the model is tuned to a point where the classical ground state is highly degenerate. In this case, two new phases emerge: a classical, finite-temperature spin liquid, characterized by a "ring" in the spin structure factor $\mathcal{S}(\mathbf{q})$; and a vortex crystal, a multiple-$Q$ state with finite magnetization, which can be viewed as an ordered lattice of magnetic vortices. All of these new phases persist for a wide range of magnetic fields. We discuss the relationship between these results and published studies of frustrated antiferromagnets, together with some of the materials where these new phases might be observed in experiment.

## I. INTRODUCTION

Much attention has been devoted to the question of whether a frustrated magnet orders or not [1]. Even in the cases where such systems do order, the results are often surprising and unconventional. Novel phases of matter have often been uncovered by applying an external magnetic field to frustrated magnet systems [2,3]. Examples of these phases range from quasiclassical magnetization plateaux and magnetic supersolid phases [4–7], magnetic analogs of liquid crystals [8–10], and crystals formed of Skyrmions, which have already been observed in experiment [11,12].

This ongoing interest in novel magnetic phases is underwritten by a steady stream of new materials. Among these, materials with frustrated ferromagnetic interactions, i.e., with ferromagnetic largest interactions but with a nonferromagnetic ground state driven by competing interactions, have a particularly rich phenomenology. Well-known examples include spin ice, a celebrated example of a three-dimensional classical spin liquid [13], and the solid phases of $^3$He, whose nuclear magnetism continues to push the limits of our understanding of quantum spins [14,15]. More recent discoveries include new families of layered, square-lattice vanadates [16–18] and cuprates [19–22], with properties that encompass ordered ground states selected by fluctuations [18], exotic singlet phases [22], helical order [21], and, surprisingly, a 1/3-magnetization plateau [20].

In this article we explore some of the novel phases which arise in a simple example of a frustrated ferromagnet: a Heisenberg model on a square lattice, in which ferromagnetic

first-neighbor interactions compete with antiferromagnetic second- and third- neighbor exchange. Using a combination of classical Monte Carlo simulation and spin-wave theory, we establish the phase diagram of this model as a function of temperature and magnetic field for two different sets of exchange parameters. In the process, we uncover a number of phases not usually associated with square-lattice magnets. These include a collinear 1/3-magnetization plateau, a spin liquid with finite magnetization, and a crystal composed of magnetic vortices. Illustrations of these phases and of the phase diagram for one of the parameter sets are shown in Figs. 1 and 2, respectively.

The model we consider is a natural generalization of the "$J_1$-$J_2$" model, which describes competing Heisenberg exchange interactions on the first- and second-neighbor bonds of a square lattice. The $J_1$-$J_2$ model has a long and interesting history and remains one of the paradigmatic examples of a frustrated magnet [24]. Much of the original interest in this model was driven by the possibility that competing antiferromagnetic exchange could stabilize a quantum spin liquid, a question which continues to inspire new research [25–28]. However, the $J_1$-$J_2$ model is also significant as a working model of magnetism in iron pnictides [29–31] and as one of the simplest possible examples of a frustrated ferromagnet. In particular, where ferromagnetic first-neighbor exchange competes with antiferromagnetic second-neighbor exchange, the spin-$\frac{1}{2}$ $J_1$-$J_2$ model can support spin-nematic order [9,32–39].

Extending frustrated spin models to include further-neighbor interactions typically results in classical ground states with incommensurate, helical order. For large values of
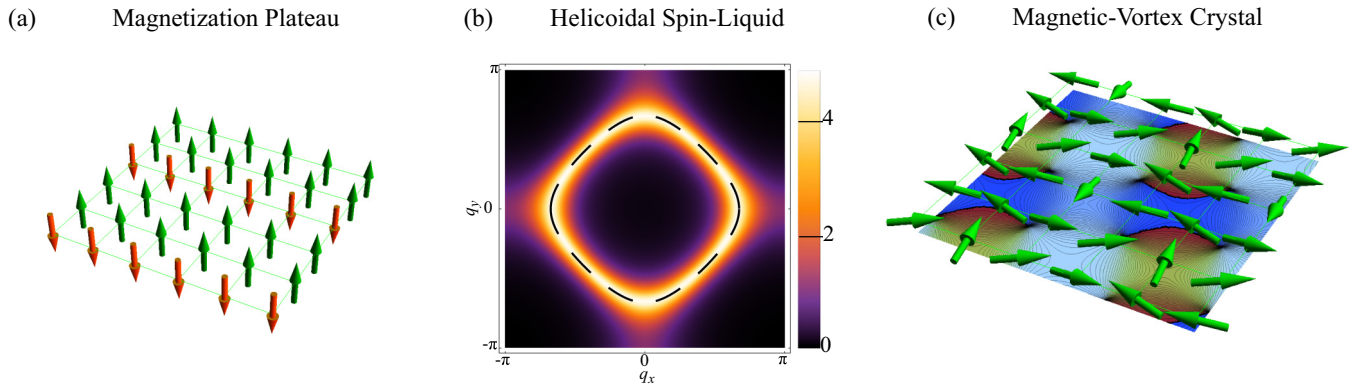
(a)    Magnetization Plateau     (b)    Helicoidal Spin-Liquid     (c)    Magnetic-Vortex Crystal



FIG. 1. Novel phases found in a square-lattice frustrated ferromagnet in applied magnetic field. (a) Collinear 1/3-magnetization plateau, with stripelike three-sublattice order. (b) Spin liquid with short-range helicoidal correlations, characterized by a "ring" in the spin structure factor $\mathcal{S}(\mathbf{q})$, shown here for $h = 0$. (c) Crystal of magnetic vortices, with finite magnetization. The color map is a representation of the phase of the spin texture in the $S^x$-$S^y$ plane. The model studied is the $J_1$-$J_2$-$J_3$ Heisenberg model on a square lattice, $\mathcal{H}_{\square}^{\mathsf{FFM}}$ [Eq. (1)].

spin, the leading effect of quantum and/or thermal fluctuations is a small correction to the pitch of the helix, leading to small, quantitative, changes in phase boundaries [40–42]. In the case of the $J_1$-$J_2$-$J_3$ Heisenberg model on a square
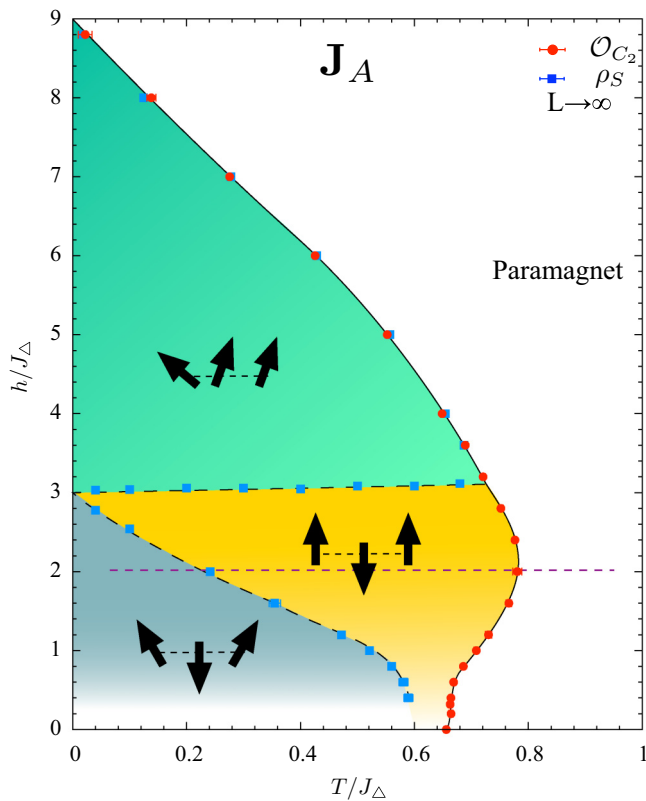


FIG. 2. Phase diagram of a square lattice frustrated ferromagnet in applied magnetic field, exhibiting the same phases as found in the Heisenberg antiferromagnet on a triangular lattice [23]: a coplanar "Y state," interpolating to "120°" order at vanishing magnetization; a collinear 1/3-magnetization plateau [cf. Fig. 1(a)]; and a coplanar 2:1 canted state. Phase boundaries are taken from classical Monte Carlo simulations of $\mathcal{H}_{\square}^{\mathsf{FFM}}$ [Eq. (1)] for the parameter set $\mathbf{J}_A$ [Eq. (18)] and scaled to the thermodynamic limit, as described in Sec. III. Temperature and magnetic field measured in units of $J_{\triangle}$ [Eq. (13)].

lattice, these expectations are borne out by linear spin-wave theory [43–45]. However, exact diagonalization calculations for $S = 1/2$ suggest a richer phase diagram, including a number of novel ground states [46,47]. Even at a classical level, other models, such as the $J_1$-$J_2$-$J_3$ Heisenberg model on a honeycomb lattice, can support a much richer behavior [48,49].

One of the possible alternatives to simple helical order are multiple-$Q$ states, composed of a coherent superposition of states with different ordering vectors. In general, these states are not compatible with the fixed spin length constraint $|\mathbf{S}| = 1$ and therefore do not belong to ground-state manifolds. However, there are a number of recent interesting cases where these phases are stabilized by the interplay between frustration and thermal fluctuations, such as the classical pyrochlore antiferromagnet [50] or the classical extended triangular-lattice antiferromagnet [51]. Interestingly, multiple-$Q$ states also arise in the description of spin textures composed of crystals of topological defects. These are the celebrated case of Skyrmion lattices in chiral magnets such as MnSi [11,12], magnetic-vortex lattices in a generic class of Mott insulators [52], or Skyrmion crystals in the antiferromagnetic triangular lattice [53]. Magnetic-vortex lattices in insulating systems seem to be especially uncommon outside the realm of superconducting systems [54,55].

The picture which emerges from the square-lattice frustrated ferromagnet studied in this article is interesting for a number of reasons. Just as in frustrated antiferromagnets, the interplay between ground-state degeneracy and fluctuations leads to a rich behavior in applied magnetic field; cf. Fig. 2. However, unlike those antiferromagnets where the frustration comes from the geometry of the lattice, the model under study here can be tuned to exhibit a wide range of different magnetic phenomena, many of them unexpected on a square lattice. This is particularly true when parameters are chosen so to place the model at the border between competing forms of order.

The remainder of this article is structured as follows.

In Sec. II we introduce the model and the methods used to study it. On the basis of known results for the classical ground state we single out two parameter sets; one which corresponds, at a mean-field level, to a triangular-lattice antiferromagnet;

and another for which the classical ground state is highly degenerate.

In Sec. III we present Monte Carlo simulation results for the first of these parameter sets. We demonstrate that the phase diagram as a function of magnetic field and temperature is almost identical to that of the Heisenberg antiferromagnet on a triangular lattice and includes its celebrated 1/3-magnetization plateau, now translated to three-sublattice order on a square lattice. These results are summarized in Fig. 2.

In Sec. IV we present Monte Carlo simulation results for the second of these parameter sets. We establish the phase diagram of a finite-size cluster as a function of magnetic field and temperature and present evidence for both a finite-temperature classical spin liquid and, at low temperature and low values of magnetic field, a multiple-$Q$ state with the character of a vortex crystal. These results are summarized in Fig. 8.

In Sec. V we discuss how these results relate to published work on frustrated antiferromagnets, how quantum effects might enter into the problem, and where these novel phases might be realized in experiment.

Finally, in Sec. VI, we conclude with a brief summary of the results and remaining open questions.

Technical details of associated spin-wave calculations, used to confirm the results of Monte Carlo simulations, are discussed in a small number of appendixes.

Appendix A develops the mathematical formalism needed to carry out both a classical low-temperature expansion and a linear spin-wave expansion about the classical ground states found in this model.

Appendix B applies this analysis to the ground-state manifold for the second parameter set and shows that thermal fluctuations select a spiral state at low temperatures and zero field, as suggested from Monte Carlo simulations.

Appendix C analyzes how, for the second parameter set, a canted $Y$ state eventually prevails over a conical version of the spiral state when a magnetic field is applied. The vortex crystal is not favored at very low temperatures, again in agreement with the Monte Carlo results.

Appendix D discusses, from linear spin-wave calculations of the quantum corrections to the ground-state energy, how the classical phase diagram for the second parameter set changes in the quantum model at low magnetic fields and temperatures.

## II. MODEL, METHOD, AND ORDER PARAMETERS

### A. The $J_1$-$J_2$-$J_3$ Heisenberg model on a square lattice

In this article, we consider one of the simplest possible prototypes for a frustrated ferromagnet, the Heisenberg model on a square lattice, with competing second- and third-neighbor exchange,

$$\mathcal{H}_{\square}^{\mathsf{FFM}} = J_1 \sum_{\langle ij \rangle_1} \mathbf{S}_i \cdot \mathbf{S}_j + J_2 \sum_{\langle ij \rangle_2} \mathbf{S}_i \cdot \mathbf{S}_j$$
$$+ J_3 \sum_{\langle ij \rangle_3} \mathbf{S}_i \cdot \mathbf{S}_j - h \sum_i S_i^z. \quad (1)$$

Here $\mathbf{S}_i$ is a classical spin with $|\mathbf{S}_i|^2 = 1$, the sum $\sum_{\langle ij \rangle_n}$ runs over the $n$th-neighbor bonds of a square lattice, as illustrated in Fig. 3, and $h$ is an applied magnetic field. We restrict ourselves to the case where first-neighbor exchange $J_1$ is
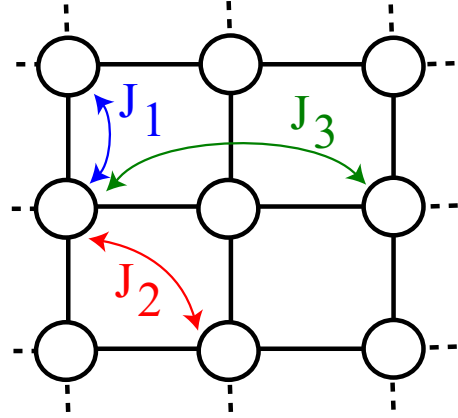


FIG. 3. Exchange interactions up to third neighbor on the square lattice. In this article we consider a Heisenberg model $\mathcal{H}_{\square}^{\mathsf{FFM}}$ [Eq. (1)] where ferromagnetic first-neighbor exchange $J_1$ competes with antiferromagnetic second- and third-neighbor exchanges $J_2$ and $J_3$.

ferromagnetic, while further-neighbor exchange $J_2$ and $J_3$ are antiferromagnetic, i.e.,

$$J_1 < 0, \quad J_2 > 0, \quad J_3 > 0. \quad (2)$$

The exchange integrals $J_1$, $J_2$, $J_3$ define a three-dimensional parameter space, and for many purposes it is convenient to represent them as a vector

$$\mathbf{J} = (J_1,\, J_2,\, J_3). \quad (3)$$

The classical ground-state phase diagram of $\mathcal{H}_{\square}^{\mathsf{FFM}}$ [Eq. (1)], together with its spin-wave excitations, was studied in a series of papers by Rastelli *et al.* [43,44] and Chubukov [45]. In the absence of magnetic field, allowing for the leading effect of fluctuations, all ground states are found to be coplanar spirals characterized by a wave vector

$$\mathbf{Q} = (Q_x, Q_y). \quad (4)$$

This wave vector can be determined by minimizing the Fourier transform of the interactions

$$J(\mathbf{q}) = 2J_1(\cos q_x + \cos q_y) + 4J_2 \cos q_x \cos q_y$$
$$+ 2J_3(\cos 2q_x + \cos 2q_y). \quad (5)$$

For ferromagnetic $J_1$ [cf. Eq. (2)], there are four distinct cases:

(1) a uniform ferromagnetic (FM) phase with

$$\mathbf{Q}^{\mathsf{FM}} = (0,0); \quad (6)$$

(2) a two-sublattice collinear antiferromagnetic (CAF) phase with

$$\mathbf{Q}^{\mathsf{CAF}} = (\pi, 0) \text{ or } (0, \pi); \quad (7)$$

(3) a family of one-dimensional (1D) spirals with

$$\mathbf{Q}^{\mathsf{1D}} = (Q_{\mathsf{1D}}, 0) \text{ or } (0, Q_{\mathsf{1D}}),$$
$$\cos Q_{\mathsf{1D}} = -\frac{J_1 + 2J_2}{4J_3}; \quad (8)$$

(4) a family of two-dimensional (2D) spirals with

$$\mathbf{Q}^{\mathsf{2D}} = (Q_{\mathsf{2D}}, Q_{\mathsf{2D}}),$$
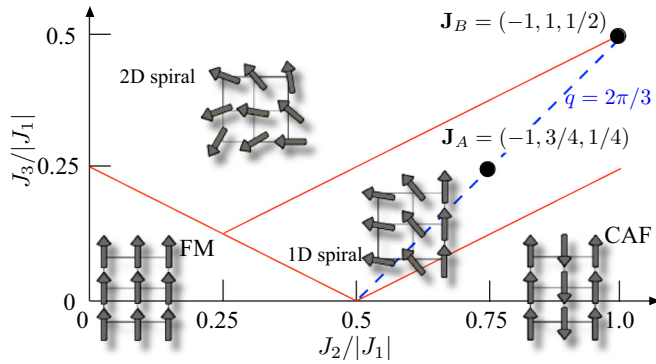$$\cos Q_{\mathsf{2D}} = -\frac{J_1}{2J_2 + 4J_3}. \quad (9)$$

FIG. 4. Classical ground-state phase diagram of the frustrated Heisenberg ferromagnet on a square lattice, $\mathcal{H}_\square^{\text{FFM}}$ [Eq. (1)], as a function of competing antiferromagnetic exchange $J_2$ and $J_3$, following [43]. Ground states in the absence of magnetic field comprise a collinear ferromagnet (FM), a collinear antiferromagnet (CAF), a one-dimensional coplanar spiral (1D spiral) and a two-dimensional coplanar spiral (2D spiral), as defined in Eqs. (6)–(9). The two parameter sets studied in this article, $\mathbf{J}_A$ [Eq. (18)] and $\mathbf{J}_B$ [Eq. (22)], are labeled with black dots. A blue dashed line indicates parameters for which the ground state is a 1D spiral with three-sublattice order [Eq. (10)].

These ground states, and the range of parameters for which they occur, are illustrated in Fig. 4.

### B. Three-sublattice order on the square lattice and its connection with a triangular-lattice antiferromagnet

In general, the one-dimensional spiral ground states of $\mathcal{H}_\square^{\text{FFM}}$ [Eq. (1)] are incommensurate with a wave vector $\mathbf{Q}^{\text{1D}}$ [Eq. (8)], which interpolates smoothly from one phase to another, e.g., from $\mathbf{Q}^{\text{FM}}$ [Eq. (6)] to $\mathbf{Q}^{\text{CAF}}$ [Eq. (7)]. For certain choices of exchange parameters, however, $\mathbf{Q}^{\text{1D}}$ takes on commensurate values. One particular case, occurring for

$$J_1 + 2J_2 - 2J_3 = 0, \quad [\, 0 < 2J_3 < |J_1| \,] \quad (10)$$

(cf. the blue dashed line in Fig. 4), is

$$\mathbf{Q}_{\text{3sub}}^{\text{1D}} = \left( \frac{2\pi}{3}, 0 \right) \text{ or } \left( 0, \frac{2\pi}{3} \right). \quad (11)$$

In this case the ground state of the frustrated ferromagnet $\mathcal{H}_\square^{\text{FFM}}$ [Eq. (1)] is composed of stripes of spins, with three-sublattice order.

Three-sublattice order also occurs in one of the paradigmatic examples of frustrated antiferromagnetism, the Heisenberg antiferromagnet on the *triangular* lattice,

$$\mathcal{H}_\triangle^{\text{AF}} = J \sum_{\langle ij \rangle} \mathbf{S}_i \cdot \mathbf{S}_j - h \sum_i S_i^z, \quad J > 0. \quad (12)$$

First studied as a potential route to a quantum spin liquid [56], this model has a long and distinguished history as a testing ground for ideas about classical and quantum magnets [3,57]. Its behavior in magnetic field, in particular, where a collinear 1/3-magnetization plateau is selected by fluctuations from a degenerate set of classical ground states [6,23,58], has come to be seen as one of the paradigms for frustrated magnets.

At a mean-field level, for a 1D spiral state with wave vector $\mathbf{Q}_{\text{3sub}}^{\text{1D}}$ [Eq. (11)], $\mathcal{H}_\square^{\text{FFM}}$ [Eq. (1)] is equivalent to $\mathcal{H}_\triangle^{\text{AF}}$ [Eq. (12)], with an effective interaction

$$J = J_\triangle = \frac{J_1 + 2J_2 + J_3}{3}. \quad (13)$$

As a consequence, the frustrated ferromagnet, $\mathcal{H}_\square^{\text{FFM}}$, inherits many of the special properties of the Heisenberg antiferromagnet on a triangular lattice. In particular, the classical ground states of $\mathcal{H}_\triangle^{\text{AF}}$ can be found by rewriting the model as

$$\mathcal{H}_\triangle^{\text{AF}} = \frac{9}{2} J_\triangle \sum_\triangle \left[ \left( \mathbf{m}_\triangle - \frac{h}{9J_\triangle} \hat{\mathbf{e}}_z \right)^2 - \frac{S^2}{3} - \frac{h^2}{81 J_\triangle^2} \right], \quad (14)$$

where $\hat{\mathbf{e}}_z$ is a unit vector in the direction of the magnetic field, the sum $\sum_\triangle$ runs over all triangles in the lattice, and

$$\mathbf{m}_\triangle = \frac{1}{3} \sum_{i \in \triangle} \mathbf{S}_i \quad (15)$$

is the magnetization *per spin* in a given triangle.

It follows from Eq. (14) that *any* state for which

$$\mathbf{m}_\triangle \equiv \frac{h}{9J_\triangle} \hat{\mathbf{e}}_z \quad \forall \, \triangle \in \text{lattice} \quad (16)$$

is a classical ground state of $\mathcal{H}_\triangle^{\text{AF}}$ and that the classical ground state interpolates to saturation (full magnetization) for a magnetic field

$$h_{\text{sat}} = 9 J_\triangle. \quad (17)$$

At a mean-field level, both of these properties carry over to three-sublattice ground states of $\mathcal{H}_\square^{\text{FFM}}$ [Eq. (1)].

However, this is by no means the end of the story; except at saturation, the mean-field constraint on $\mathbf{m}_\triangle$ [Eq. (16)] *does not* uniquely constrain the ground state, and fluctuations play a crucial role in establishing order. In the case of the Heisenberg antiferromagnet on a triangular lattice, $\mathcal{H}_\triangle^{\text{AF}}$ [Eq. (12)], it is known that thermal [6,23,59] and/or quantum [60] fluctuations act on the large family of degenerate three-sublattice ground states to select

(i) a coplanar 120° state with zero magnetization, for $h = 0$;

(ii) a coplanar $Y$ state with finite magnetization, interpolating to 120° order for $h \to 0$;

(iii) a collinear "uud" state associated with a 1/3-magnetization plateau for intermediate values of $h$;

(iv) a coplanar 2:1 canted state, interpolating between the 1/3-magnetization plateau and the saturated state for $h \to h_{\text{sat}}$.

The associated classical phase diagram is shown in Fig. 1 of Ref. [23]. Since strict long-range order of phases which break a continuous symmetry is forbidden at finite temperature in two dimensions by the Mermin-Wagner theorem, the coplanar phases should be understood as algebraically correlated.

In Sec. III we use classical Monte Carlo simulation to explore how the equivalent three-sublattice order in the square-lattice frustrated ferromagnet $\mathcal{H}_\square^{\text{FFM}}$ [Eq. (1)] evolves as a function of temperature and magnetic field. For these purposes, we select the parameter set

$$\mathbf{J}_A = (J_1, J_2, J_3) = (-1, 3/4, 1/4), \quad (18)$$

marked with a black dot in Fig. 4, as representative of parameters with a three-sublattice ground state [cf. Eq. (10)]. This, in turn, sets a characteristic scale for temperature and magnetic field through Eq. (13).

### C. Highly degenerate manifold of classical ground states

An enlarged ground-state manifold occurs where the 1D and 2D spirals meet, for

$$J_2 - 2J_3 = 0 \quad \forall \; |J_1| < 4J_2 < 4|J_1| \tag{19}$$

(cf. Fig. 4). On this phase boundary, the classical ground states of $\mathcal{H}_\square^{\mathrm{FFM}}$ are 2D spirals with wave vector

$$\mathbf{Q}^{\mathrm{ring}} = \left( Q_x^{\mathrm{ring}}, \, Q_y^{\mathrm{ring}} \right),$$
$$Q_y^{\mathrm{ring}} = \pm \arccos \left( \frac{-J_1}{2J_2} - \cos Q_x^{\mathrm{ring}} \right), \tag{20}$$

which interpolates from the 1D to the 2D spiral. This set of $\mathbf{Q}$ forms a ring in reciprocal space, centered on

$$\Gamma = (0, 0), \tag{21}$$

and defines a highly degenerate manifold of states.

In Sec. IV we use classical Monte Carlo simulation to explore the consequences of this enlarged ground-state degeneracy at finite temperature and magnetic field. We consider the limiting case where the line Eq. (10), corresponding to a 1D spiral with three-sublattice order, terminates at the phase boundary between 1D and 2D spirals at

$$\mathbf{J}_B = (J_1, \, J_2, \, J_3) = (-1, \, 1, \, 1/2). \tag{22}$$

This parameter set is denoted as a black dot in Fig. 4. The set of ground-state wave vectors $\mathbf{Q}^{\mathrm{ring}}$ [Eq. (20)] at $\mathbf{J}_B$ is shown as a dashed line in Fig. 1(b).

### D. Monte Carlo simulation method

In Secs. III and IV of this paper, we use large-scale Monte Carlo simulation to study the finite-temperature properties of the square-lattice frustrated ferromagnet $\mathcal{H}_\square^{\mathrm{FFM}}$ [Eq. (1)] in applied magnetic field. Simulations were performed using parallel tempering [61], using 48 to 80 replicas (temperatures). Simulations were carried out for square clusters of

$$N = L \times L \tag{23}$$

spins, with periodic boundary conditions. The linear sizes $L$ were chosen to be commensurate with possible $\mathbf{Q}$ wave vectors in the range $60 \leqslant L \leqslant 180$. Typical simulations involved $2 \times 10^6$ steps, half of which were discarded for thermalization. At every ten steps there was an attempt at exchanging replicas at neighboring temperatures. Energy scales (field and temperature) were normalized to $J_\triangle$ [Eq. (13)] for easy comparison with the triangular lattice antiferromagnet [23].

The simulations for the parameter set $\mathbf{J}_B$ [Eq. (22)], presented in Sec. IV, become very challenging at low temperatures, especially for low values of magnetic field, where several different phases compete. In this case we performed different simulation runs, with and without parallel tempering, where the initial state was either one of the candidate phases at $T = 0$ or a configuration composed of domains of different phases, in order to ascertain their relative stability.

### E. A short catalog of order parameters and correlation functions

Experience of simulating the Heisenberg antiferromagnet on a triangular lattice (Ref. [23]), together with the symmetry of the ordered phases found in the absence of magnetic field (cf. Fig. 4), suggests a number of order parameters and correlation functions likely to be of use in determining the behavior of $\mathcal{H}_\square^{\mathrm{FFM}}$ [Eq. (1)] in applied magnetic field.

The 1D spiral phase in Fig. 4 breaks the fourfold rotational symmetry of the square lattice from $C_4$ down to $C_2$ by choosing to orient the stripes in vertical or horizontal direction. We analyze this with the following order parameter:

$$\mathcal{O}_{C_2} = \langle |\phi_\mathbf{x}| \rangle, \tag{24}$$

$$\phi_\mathbf{x} = \frac{9}{32N} \sum_i \mathbf{S}_i \cdot (\mathbf{S}_{i+\hat{\mathbf{x}}} - \mathbf{S}_{i+\hat{\mathbf{y}}}). \tag{25}$$

The sum over $i$ runs over all $N = L^2$ lattice sites and the lattice unit vectors are denoted as $\hat{\mathbf{x}} = (1,0)$ and $\hat{\mathbf{y}} = (0,1)$.

In the presence of field, the three-sublattice ordered states break the translational symmetry of the lattice along the $S^z$ direction. This can be measured by an order parameter based on a two-dimensional irreducible representation of $C_3 \cong \mathbb{Z}_3$; cf. the triangular-lattice case [23],

$$\psi_{\mathbf{x},1}^z = \frac{3}{\sqrt{6}N} \sum_i 2S_i^z + 2S_{i+\hat{\mathbf{x}}}^z - 4S_{i+2\hat{\mathbf{x}}}^z, \tag{26}$$

$$\psi_{\mathbf{x},2}^z = -\frac{3}{\sqrt{2}N} \sum_i 2S_{i+\hat{\mathbf{x}}}^z - 2S_i^z, \tag{27}$$

where the sum over $i$ runs over the $N/3$ "three-spin stripes," each equivalent to an elementary triangle. In order to account for the two ways of breaking the $C_2$ symmetry, the $\mathbb{Z}_3$ order parameter must be measured along both directions of the lattice, i.e., $\hat{\mathbf{x}} \to \hat{\mathbf{y}}$ in Eqs. (26) and (27). The resulting final order parameter is

$$\mathcal{O}_{\mathbb{Z}_3}^z = \left\langle \left[ \left| \psi_{\mathbf{x},1}^z \right|^2 + \left| \psi_{\mathbf{x},2}^z \right|^2 + \left| \psi_{\mathbf{y},1}^z \right|^2 + \left| \psi_{\mathbf{y},2}^z \right|^2 \right]^{1/2} \right\rangle. \tag{28}$$

The susceptibility associated with each order parameter $\mathcal{O}$ is defined as

$$\chi = N \frac{\langle |\mathcal{O}|^2 \rangle - \langle |\mathcal{O}| \rangle^2}{T}. \tag{29}$$

In the presence of magnetic field, quasi-long-range order can develop in the transverse components of spin

$$\mathbf{S}_i^\perp = \left( S_i^x, S_i^y \right). \tag{30}$$

This is captured by the spin stiffness $\rho_S$ (see, e.g., Refs. [23,62] and references therein),

$$\rho_s[\hat{\mathbf{e}}] = \frac{1}{N} \left\langle \sum_\delta J_\delta \sum_{\langle i,j \rangle_\delta} (\hat{\mathbf{e}} \cdot \mathbf{r}_{ij})^2 \mathbf{S}_i^\perp \cdot \mathbf{S}_j^\perp \right\rangle$$
$$- \frac{1}{NT} \left\langle \left( \sum_\delta J_\delta \sum_{\langle i,j \rangle_\delta} (\hat{\mathbf{e}} \cdot \mathbf{r}_{ij}) \mathbf{S}_i^\perp \times \mathbf{S}_j^\perp \right)^2 \right\rangle, \tag{31}$$

which is averaged over the two lattice directions $\hat{\mathbf{e}} = \{\hat{\mathbf{x}}, \hat{\mathbf{y}}\}$.

The specific heat, defined as

$$C_h = \frac{1}{N} \frac{\langle E \rangle - \langle E \rangle^2}{T^2}, \qquad (32)$$

where $E$ is the total internal energy, is also helpful in tracking phase transitions.

Last, but not least, the momentum-resolved spin structure factor

$$\mathcal{S}(\mathbf{q}) = \left\langle \frac{1}{N} \left| \sum_i \mathbf{S}_i \exp(-i\mathbf{q} \cdot \mathbf{r}_i) \right|^2 \right\rangle \qquad (33)$$

is of considerable importance for characterizing the spin-liquid phase studied in Sec. IV. Where appropriate, we analyze separately the structure factors for the longitudinal and transverse components of spin,

$$\mathcal{S}^z(\mathbf{q}) = \left\langle \frac{1}{N} \left| \sum_i S_i^z \exp(-i\mathbf{q} \cdot \mathbf{r}_i) \right|^2 \right\rangle, \qquad (34)$$

$$\mathcal{S}^\perp(\mathbf{q}) = \left\langle \frac{1}{N} \left| \sum_i \mathbf{S}_i^\perp \exp(-i\mathbf{q} \cdot \mathbf{r}_i) \right|^2 \right\rangle, \qquad (35)$$

where $\mathbf{S}^\perp$ is defined in Eq. (30).

## III. TRIANGULAR-LATTICE PHYSICS ON A SQUARE LATTICE

In Sec. II B, we established a connection between the square-lattice frustrated ferromagnet, $\mathcal{H}_\square^{\mathrm{FFM}}$ [Eq. (1)], and the Heisenberg antiferromagnet on a triangular lattice, $\mathcal{H}_\triangle^{\mathrm{AF}}$ [Eq. (12)], in the case where the ground state of $\mathcal{H}_\square^{\mathrm{FFM}}$ is a 1D-spiral with wave vector

$$\mathbf{Q}_{3\mathrm{sub}}^{1\mathrm{D}} = \left( \frac{2\pi}{3}, 0 \right) \text{ or } \left( 0, \frac{2\pi}{3} \right)$$

[cf. Eq. (11)], corresponding to three-sublattice "stripe" order. An example of a three-sublattice stripe state, with finite magnetization, is shown in Fig. 1(a). The momentum set of the ground-state manifold,

$$Q_\triangle = \{(\pm 2\pi/3, 0), \ (0, \pm 2\pi/3)\}, \qquad (36)$$

has four components, whereas that of the triangular antiferromagnet has only two.

In what follows, we use classical Monte Carlo simulation to explore the properties of $\mathcal{H}_\square^{\mathrm{FFM}}$ at finite temperature and magnetic field, considering a parameter set $\mathbf{J}_A$ [Eq. (18)]. The results of these simulations are summarized in the phase diagram Fig. 2. The similarities to the magnetic phase diagram of the triangular-lattice antiferromagnet $\mathcal{H}_\triangle^{\mathrm{AF}}$ (cf. Fig. 1 of [23]) are striking. At first sight, the main difference is only that the ordering temperature scale is roughly double that for $\mathcal{H}_\square^{\mathrm{FFM}}$. As in the case of the triangular-lattice antiferromagnet [23], it will be instructive to compare the phase diagram where a proper finite-size scaling has been performed (Fig. 2) to one extracted from simulations of a fixed cluster size $L = 90$ (Fig. 5).

While the two models have much in common, differences arise in the way in which ordered phases break lattice symmetries. In both cases, under applied magnetic field,
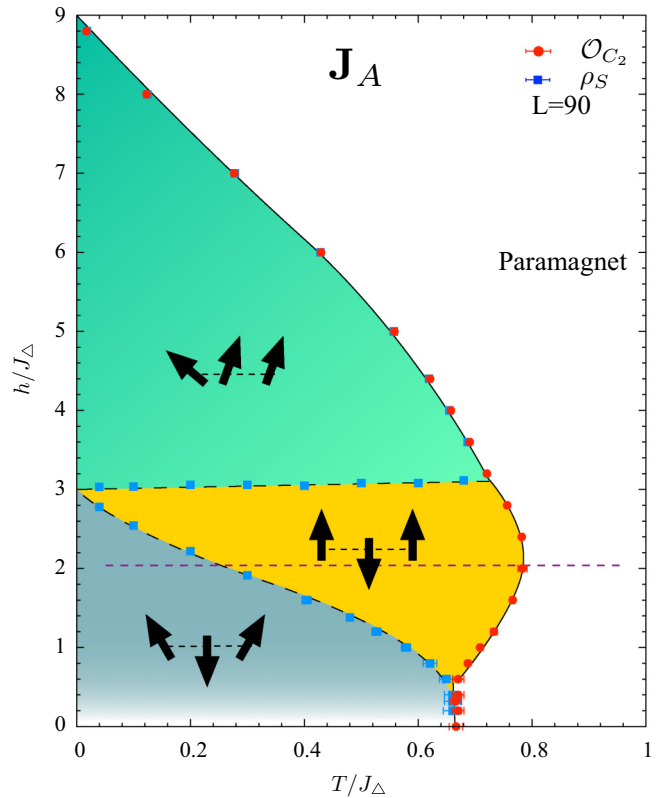


FIG. 5. Finite-size phase diagram of a square-lattice frustrated ferromagnet in applied magnetic field. The phases found—a coplanar $Y$ state; a collinear 1/3-magnetization plateau; and a coplanar 2:1 canted state—and the structure of the phase diagram closely parallel finite-size results for the Heisenberg antiferromagnet on a triangular lattice [23]. In both cases, finite-size effects strongly renormalize the temperature associated with the transition from the collinear 1/3-magnetization plateau into the $Y$ state. Results are taken from classical Monte Carlo simulations of $\mathcal{H}_\square^{\mathrm{FFM}}$ [Eq. (1)] for the parameter set $\mathbf{J}_A$ [Eq. (18)]. Phase boundaries were extracted from anomalies in the order parameter associated with lattice rotations [Eq. (24)] and spin stiffness $\rho_S$ [Eq. (30)] for a cluster of $N = 90^2 = 8100$ spins. Temperature and magnetic field are measured in units of $J_\triangle$ [Eq. (13)]. The horizontal dashed line corresponds to the temperature cut used in Fig. 7.

three-sublattice ordered phases break a discrete $C_3 \cong \mathbb{Z}_3$ symmetry, associated with the interchange of the different sublattices. However, the stripelike order found in the square-lattice model also breaks a $C_2$ lattice-rotation symmetry when choosing between the two possible ordering vectors, $\mathbf{Q}_{3\mathrm{sub}}^{1\mathrm{D}}$ [Eq. (11)]. This additional symmetry has a number of interesting consequences, described below.

### A. Ising transition at $h = 0$

We consider first the limit of vanishing magnetic field, corresponding to $h/J_\triangle = 0$ in Fig. 2. In the absence of magnetic field, the Heisenberg antiferromagnet on a triangular lattice $\mathcal{H}_\triangle^{\mathrm{AF}}$ [Eq. (12)] has been argued to exhibit a finite-temperature transition, linked with the proliferation of $\mathbb{Z}_2$ vortices associated with spin chirality [63]. Whether this
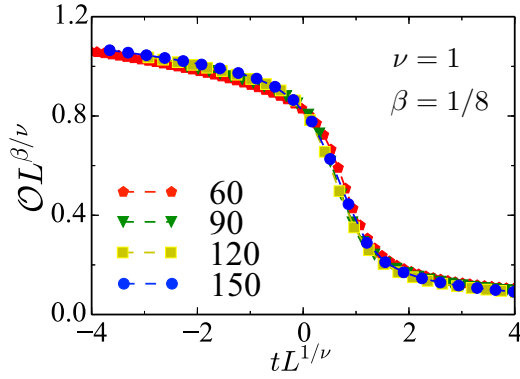
FIG. 6. Finite-temperature phase transition into a three-sublattice, 120° ground state, breaking lattice-rotation symmetry. The order parameter $\mathcal{O}_{C_2}$ [Eq. (24)] shows finite-size scaling consistent with a phase transition in the Ising universality class, in contrast with the triangular-lattice Heisenberg model [63]. Results are taken from classical Monte Carlo simulations of $\mathcal{H}_{\square}^{\mathrm{FFM}}$ [Eq. (1)] for the parameter set $\mathbf{J}_A$ [Eq. (18)] in the absence of magnetic field ($h = 0$).

process corresponds to either a true phase transition or a crossover is still under debate [64–67].

The situation in the square-lattice frustrated ferromagnet $\mathcal{H}_{\square}^{\mathrm{FFM}}$ [Eq. (1)] is quite different. At $h = 0$, a clear phase transition is observed, associated with the breaking of lattice-

rotation symmetry by three-sublattice stripe order. The relevant order parameter is $\mathcal{O}_{C_2}$ [Eq. (24)], and in Fig. 6 we show a scaling plot of simulation results for

$$\mathcal{O}_{C_2} = L^{-\beta/\nu}\tilde{\mathcal{O}}(tL^{1/\nu}), \tag{37}$$

as a function of the reduced temperature,

$$t = \frac{T_c - T}{T}, \tag{38}$$

where the Ising critical exponents

$$\nu = 1, \quad \beta = \tfrac{1}{8}, \tag{39}$$

are found to describe the data well.

We do not observe behavior explicitly related to the unbinding of $\mathbb{Z}_2$ vortices in simulation of $\mathcal{H}_{\square}^{\mathrm{FFM}}$. However, just as in simulations of $\mathcal{H}_{\triangle}^{\mathrm{AF}}$ (cf. Ref. [23]), the correlation length associated with transverse components of spin becomes very large as $h \to 0$, making it difficult to draw definitive conclusions.

### B. Double transition for $0 \lesssim h \leqslant 3J_\triangle$

We now consider the phases found for low to intermediate values of magnetic field in the phase diagram Fig. 2. Here a double phase transition is observed as the system is cooled down from the paramagnet; cf. Fig. 7, for $0 \lesssim h/J_\triangle \leqslant 3$. As the system is cooled from the high-temperature paramagnet,
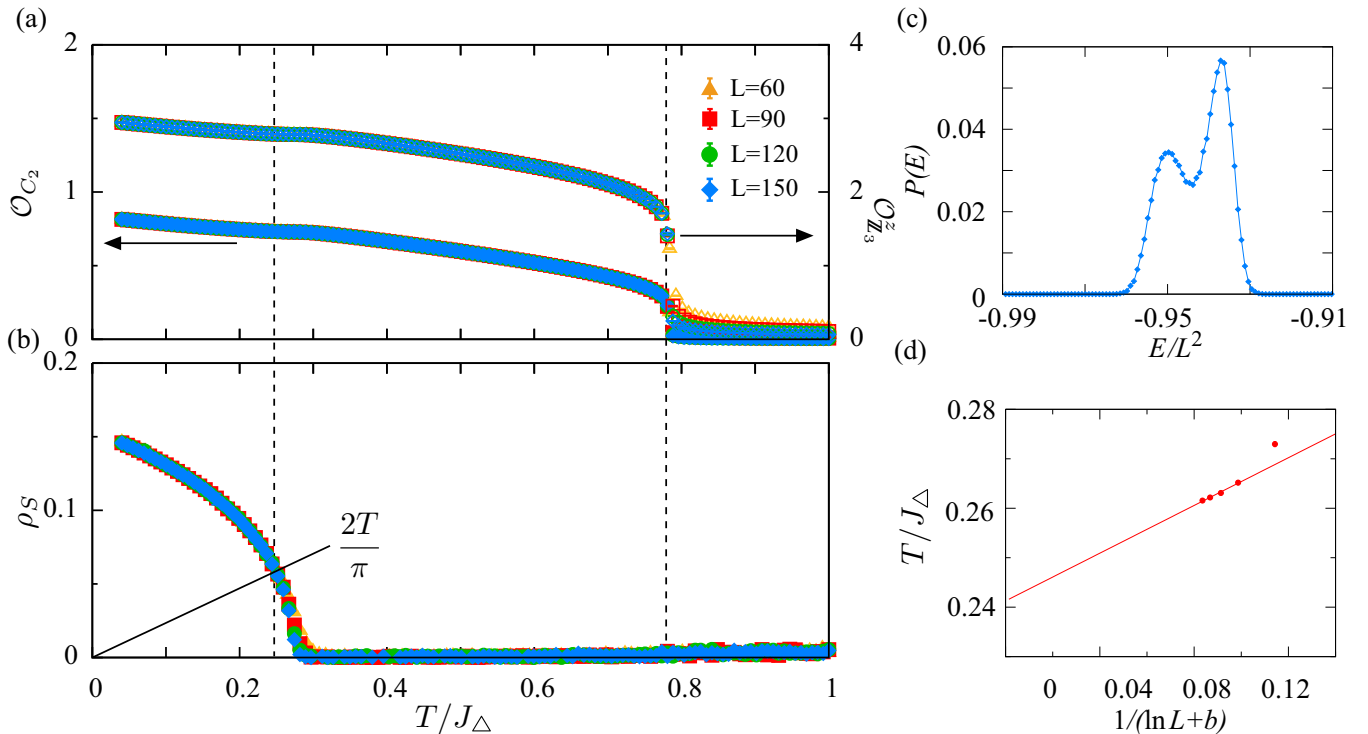


FIG. 7. Evidence for a collinear 1/3-magnetization plateau and coplanar Y state in a square-lattice frustrated ferromagnet. (a) Temperature dependence of the order parameters $\mathcal{O}_{C_2}$ [Eq. (24)] and $\mathcal{O}_{\mathbb{Z}_3}^z$ [Eq. (28)], showing the onset of a collinear state with three-sublattice stripe order (1/3-magnetization plateau), at $T \approx 0.78J_\triangle$. (b) Temperature dependence of the spin stiffness $\rho_S$ [Eq. (31)], consistent with a Berezinski-Kosterlitz-Thouless (BKT) transition into the Y state at $T_L \approx 0.24J_\triangle$. (c) Energy histogram calculated for $T = 0.776J_\triangle$, showing the discontinuous nature of the phase transition from paramagnet to 1/3-magnetization plateau. (d) Finite-size scaling of the temperature associated with the BKT transition, $T_L$ [Eq. (41)]. Results are taken from classical Monte Carlo simulations of $\mathcal{H}_{\square}^{\mathrm{FFM}}$ [Eq. (1)] for the parameter set $\mathbf{J}_A$ [Eq. (18)] in applied magnetic field $h/J_\triangle = 2$; cf. dashed line in Fig. 5. Temperature is measured in units of $J_\triangle$ [Eq. (13)].

it first enters the collinear 1/3-magnetization plateau, as described by the rise of the order parameters in Fig. 7(a). This process is a single phase transition, which simultaneously breaks the $C_2$ lattice-rotational symmetry [Eq. (24)] and the $\mathbb{Z}_3$ translational symmetry [Eq. (28)] associated with the three-sublattice order. For values of magnetic field $1.5 \lesssim h/J_\triangle < 3$, a double distribution in the internal energy is clearly observed at the transition temperature [Fig. 7(c)], which shows that the transition is of first order. We cannot observe this behavior for lower magnetic fields, presumably due to the increased finite-size effects.

In the case of the Heisenberg antiferromagnet on a triangular lattice, different 1/3-magnetization plateau states are connected by a threefold permutation symmetry, and the phase transition into the paramagnet is continuous [23]. Meanwhile, in the case of the square-lattice frustrated ferromagnet, the permutation of different sublattices is complemented by a lattice rotation, enlarging the symmetry from $\mathbb{Z}_3$ to $\mathbb{Z}_2 \times \mathbb{Z}_3$, and the corresponding phase transition is first order. This is reminiscent of the six-state Potts model in 2D, whose ordering phase transition is known to be first order [68,69].

The canted $Y$ state is found by lowering the temperature further from the plateau phase. In addition to breaking the $C_2$ and $\mathbb{Z}_3$ symmetries, this phase displays algebraic order in the $S^x$-$S^y$ plane, as shown by the finite spin stiffness in Fig. 7(b). Assuming a Berezinski-Kosterlitz-Thouless (BKT) transition [70], the transition temperature in a finite-size system is found via the jump in spin stiffness,

$$T_L = \frac{\pi}{2} \times \Delta\rho_S, \tag{40}$$

which can then be finite-size scaled in a characteristic logarithmic fashion [23,71],

$$T_L = T_{\text{BKT}}\left(1 + \frac{1}{2}\frac{1}{\ln L + \ln b}\right), \tag{41}$$

as shown in Fig. 7(d).

The finite-size corrections to this transition are observed to be rather large. From simulations of a fixed cluster size $L$, cf. the phase diagram for $L = 90$ in Fig. 5, it is unclear if the BKT transition merges with the $C_2 \otimes \mathbb{Z}_3$ transition for fields $h \lesssim 0.6$, i.e., if there is a single transition from the paramagnet to the $Y$ state, or two. However, these two phase transitions are observed to be clearly separated once the proper finite-size scalings are performed, and no direct transition from the paramagnet into the $Y$ phase can be reported for fields $h \geqslant 0.4 J_\triangle$ (Fig. 2). We have faded the region in Fig. 2 corresponding to values of field $0 < h \leqslant 0.4 J_\triangle$, since finite-size effects become very large in this region and this analysis becomes unreliable. However, the available data still suggest the presence of a double phase transition as the field approaches $h \to 0$. This behavior very closely matches what is observed in the Heisenberg antiferromagnet on a triangular lattice, which has been discussed in detail previously [23].

For magnetic fields above the plateau $h > 3 J_\triangle$, we register a single phase transition into the 2:1 canted state. The location of several quantities, such as the jump in the spin stiffness and anomalies in the $C_2$ and $\mathbb{Z}_3$ order-parameter susceptibilities and in the specific heat, coincide within resolution after they are properly finite-size scaled. We do not observe any discon-tinuity in the internal energy as a function of temperature, or a bimodal energy distribution at the transition temperature, in the clusters simulated. Nonetheless, the maximum value of the specific heat scales roughly with $N$, and the temperature at which it is found scales roughly with $1/N$, behaviour consistent with a first-order transition.

## IV. CONSEQUENCES OF AN ENLARGED GROUND-STATE MANIFOLD

We now consider the properties of $\mathcal{H}_\square^{\text{FFM}}$ [Eq. (1)] for the parameter set $\mathbf{J}_B$ [Eq. (22)], as summarized in the phase diagram, Fig. 8. This parameter set corresponds to the point in the classical ground-state phase diagram (Fig. 4) where the line of 1D spirals with three-sublattice order terminates on the boundary with the 2D spiral phase. The behavior of the model at this special point is determined by the highly degenerate
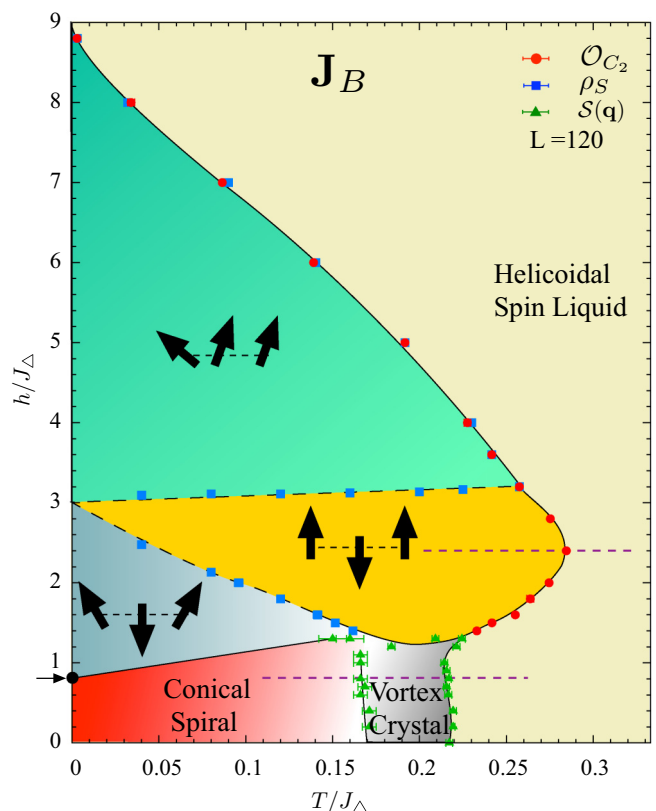


FIG. 8. Finite-size phase diagram of a square-lattice frustrated ferromagnet in applied magnetic field, showing a classical spin liquid and, at low fields, a vortex crystal [cf. Fig. 1(c)]. The other phases found are a conical-spiral state interpolating to zero magnetization; a coplanar $Y$ state and a collinear 1/3-magnetization plateau [cf. Fig. 1(a)] at intermediate magnetization; and a coplanar 2:1 canted state interpolating to saturation. Results are taken from classical Monte Carlo simulations of $\mathcal{H}_\square^{\text{FFM}}$ [Eq. (1)] for the parameter set $\mathbf{J}_B$ [Eq. (22)], corresponding to a point of high degeneracy. Phase boundaries were extracted from anomalies in the order parameter associated with lattice rotations [Eq. (24)], spin stiffness $\rho_S$ [Eq. (30)], and the spin structure factor $\mathcal{S}(\mathbf{q})$ [Eq. (33)] for a cluster of $N = L^2 = 120^2 = 14\,400$ spins. Temperature and magnetic field are measured in units of $J_\triangle$ [Eq. (13)]. The horizontal dashed lines corresponds to the temperature cuts used in Figs. 9–13 and Fig. 14.
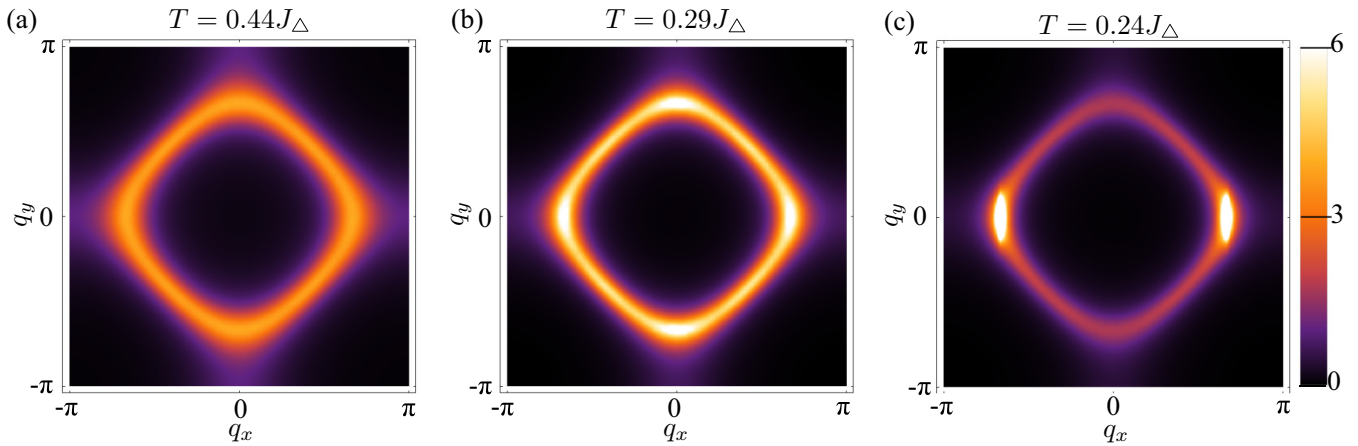
FIG. 9. Transition from the helicoidal spin liquid into a collinear $m = 1/3$ magnetization plateau, in applied magnetic field, as revealed by the spin structure factor $\mathcal{S}(\mathbf{q})$ [Eq. (33)]. (a) Spin correlations for $T = 0.44 J_\triangle$, showing a ring feature characteristic of the high-temperature spin liquid. (b) Spin correlations for $T = 0.29 J_\triangle$, approaching the transition into an ordered state, showing an enhancement of fluctuations near to potential ordering wave vectors. (c) Spin correlations for $T = 0.24 J_\triangle$, within the collinear $m = 1/3$ magnetization plateau, showing Bragg peaks at $\mathbf{Q}_{3\text{sub}}^{1D}$ [Eq. (11)], coexisting with the ring feature. Results are taken from classical Monte Carlo simulations of $\mathcal{H}_\square^{\text{FFM}}$ [Eq. (1)], for a cluster of $L^2 = 90^2$ spins, with exchange parameters $\mathbf{J}_B$ [Eq. (22)]. Magnetic field was set to $h = 2.4 J_\triangle$, corresponding to the dashed in line in Fig. 8. The $\mathbf{q} = 0$ component of the spin correlations has been subtracted for clarity.

manifold of states described in Sec. II C. As we shall see, the ring structure defined in Eq. (20) leaves a characteristic fingerprint in the spin structure factor for all temperatures and values of magnetic field.

For a generic choice of parameters on the boundary between 1D and 2D spirals, it is not possible to find commensurate wave vectors $\mathbf{Q}$ which satisfy Eq. (20). However, for specific choices of parameters $\mathbf{J}$, commensurate wave vectors do exist, and the parameter set which offers the greatest number of commensurate states is, in fact, set $\mathbf{J}_B$. Here the wave vectors

$$\mathbf{Q}_R = \{(0, 2\pi/3), (\pi/2, \pi/3), (\pi/5, 3\pi/5)\}, \qquad (42)$$

together with their reflections and mirrors, fulfill Eq. (20). In total, this gives 20 different commensurate wave vectors, compatible with a wide range of cluster sizes.

We begin by establishing the finite-temperature phase diagram (Fig. 8) using Monte Carlo simulations for a cluster of size $L = 120$. For values of applied field $h \gtrsim 1.2 J_\triangle$, the phase diagram closely follows that of the parameter set $\mathbf{J}_A$ [Eq. (18)] (and therefore the Heisenberg antiferromagnet on a triangular lattice, $\mathcal{H}_\triangle^{\text{AF}}$ [Eq. (12)]), displaying the succession of canted $Y$ phase, collinear 1/3-magnetization plateau, and canted 2:1 phase as a function of increasing magnetic field.

Simulations become very challenging at lower values of applied field, $h \lesssim 1.2 J_\triangle$, making it very difficult to extrapolate results to the thermodynamic limit. Still, in this region we can establish the presence of two additional noncoplanar phases. At very low temperatures, a conical-spiral phase described by a single wave vector is favored by thermal fluctuations, as described in Sec. IV B. At intermediate temperatures, between this phase and the disordered paramagnet phase, a novel conical phase, with a more complex spin texture, is stabilized, as described in Sec. IV C; cf. Fig. 1(c).

All the ordered phases at $\mathbf{J}_B$ are described by wave vectors belonging to, or combinations of, $\mathbf{Q}_R$ [Eq. (42)]. All the transitions from the disordered phase are very clearly observed

to be of first order. The overall ordering-temperature scale is strongly reduced from the $\mathbf{J}_A$ case, in units of both $J_\triangle$ and $|J_1|$, indicating the larger role played by frustration in this case, suppressing the ordering tendency of the model.

### A. Spin-liquid phase from a ring of correlations

We consider first the nature of the paramagnetic phase found for all values of magnetic field at sufficiently high temperature, as shown in the phase diagram Fig. 8. The highly degenerate ground-state manifold of $\mathcal{H}_\square^{\text{FFM}}$ at the parameter set $\mathbf{J}_B$ [Eq. (22)] is not just of concern at $T = 0$, but also has profound consequences at finite temperature. Its effects are most obvious in the spin structure factor $\mathcal{S}(\mathbf{q})$ [Eq. (33)], which takes on a finite value for all wave vectors $\mathbf{q}$ which satisfy, or nearly satisfy, the ring condition Eq. (22). A corresponding ring structure can be seen in $\mathcal{S}(\mathbf{q})$ for *all* of the ordered phases shown in Fig. 8 and is equally prominent for $h = 0$ [Fig. 1(b)] and for $h = 2.4 J_\triangle$ (Fig. 9). In the paramagnetic regions of the phase diagram (Fig. 8), where no symmetries are broken, the extra degeneracy gives rise to a classical spin liquid.

The nature of the correlations along the ring does not change in any fundamental way when magnetic field is applied. In Fig. 9 we show the evolution of the full structure factor $\mathcal{S}(\mathbf{q})$ at $h = 2.4 J_\triangle$ as the temperature is lowered from the disordered phase into the 1/3-magnetization plateau. At high temperatures and away from the transition [Fig. 9(a)], the height of $\mathcal{S}(\mathbf{q})$ is very uniform, such that many wave vectors belonging to the ring, or very close to it, contribute equally. If the temperature is raised from this point, the height of $\mathcal{S}(\mathbf{q})$ just decreases smoothly, and no crossover into a standard paramagnet is observed at any temperature scale. When the system is cooled down to near the phase transition $T \approx 0.29 J_\triangle$ [Fig. 9(b)], peaks begin to develop at the wave vectors $Q_\triangle$ [Eq. (36)], corresponding to incipient three-sublattice magnetic order. Inside the magnetization plateau at even lower temperature [Fig. 9(c)], Bragg peaks [from the $\mathcal{S}^z(\mathbf{q})$
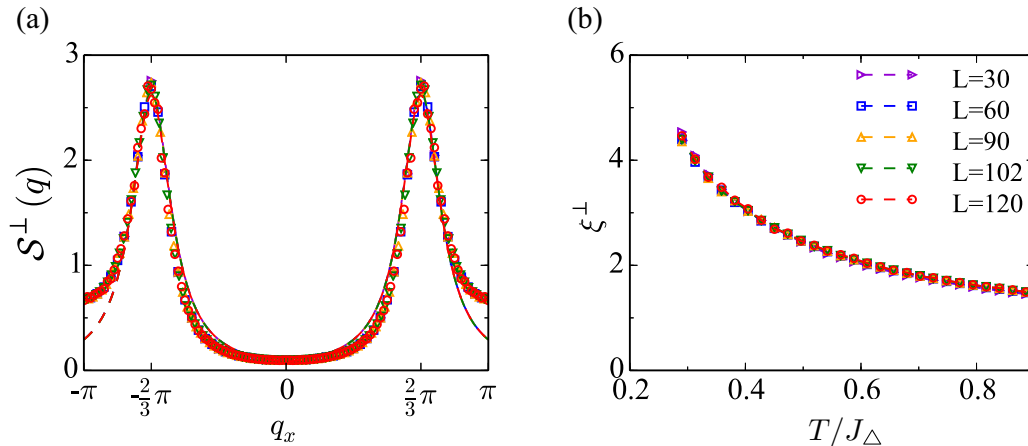
FIG. 10. Characterization of the helicoidal spin liquid in applied magnetic field $h = 2.4J_\triangle$. (a) Structure factor $\mathcal{S}^\perp(q_x, 0)$ [Eq. (35)], showing a cross section of the characteristic ring of scattering [cf. Fig. 9(a)]. Data for a wide range of system sizes collapse onto a single curve. Dashed lines are fits to a Lorentzian [Eq. (43)], from which the correlation length $\xi$ is obtained. (b) Temperature dependence of the correlation length $\xi$. Results are taken from classical Monte Carlo simulations of $\mathcal{H}_\square^{\mathrm{FFM}}$ [Eq. (1)], for clusters of $N = L \times L$ spins, with $T = 0.45J_\triangle$ and the same values of exchange and magnetic field as Fig. 9.

component of the structure factor] are observed, associated with the broken $\mathbb{Z}_3$ symmetry discussed in Sec. III. A diffuse ring of low-lying excitations can still be observed in this phase, attesting to the pervasiveness of the ring correlations.

In order to further clarify the physical implications of this ring in the structure factor, we now focus on the transverse component $\mathcal{S}^\perp(\mathbf{q})$ [Eq. (35)]. Figure 10(a) shows a cut of $\mathcal{S}^\perp(\mathbf{q})$ along the line $q_y = 0$ in the disordered phase for $h = 2.4J_\triangle$ and $T = 0.45J_\triangle$. We find that the structure factor can be fitted quite well to a (double) Lorentzian expression of the form

$$\mathcal{S}^\perp(q) = \frac{A^2}{\xi^{-2} + (q - q_0)^2}, \tag{43}$$

centred at $q_0 = \pm 2\pi/3$. Similar fits can be performed for different cuts of $\mathcal{S}^\perp(\mathbf{q})$ in the $Q_x$-$Q_y$ plane.

The width of the structure factor around $q_0$ is controlled by the correlation length $\xi$, which sets a finite length scale for correlations. $\mathcal{S}^\perp(q)$ shows practically no finite-size dependence for the clusters studied, attesting to the short-range nature of the correlations. The correlation length $\xi$ decays slowly with temperature [Fig. 10(b)], which indicates the stability of the ring correlations for a wide range of temperatures.

Our next target is the *total* structure factor arising from low-energy excitations associated with the ring. First, we need identify the wave vectors $\mathbf{Q}_{\mathrm{ring}}$ contributing to the total ring structure factor. A finite $\xi$ means that there are momenta outside the $T = 0$ ring [Eq. (20)] which will contribute to the total structure factor [cf. Fig. 1(b)]. In order to capture these wave vectors with a finite spectral weight, we take the one-sublattice spin-wave dispersion Eq. (A57) [see Appendix A] and impose an energy cutoff of $\omega_c = 0.01J_\triangle$ on it. Alternatively, using the inverse of the correlation length of Fig. 10(b) as input, we can predict approximately the wave vectors which will be thermally activated. Both approaches provide the same set of wave vectors belonging to the enlarged ring, but the latter, correlation-length-based method becomes unwieldy and computationally more expensive for large system sizes.

The number of momentum vectors, $N_R$, thermally activated is found to scale *linearly* with the cluster size $N_R \sim L^2$, for a very wide range of system sizes (Fig. 11). The area covered by the ring is given roughly by the product of its width with its perimeter, which scales with $L$. This implies that there are approximately $L$ cuts across the ring such as Fig. 10(a). The ring has a fixed width in momentum space, set by $\xi^{-1}$, which is basically independent of $L$; see Fig. 10(b). Since the resolution in momentum space scales with system size as $L^{-1}$, the number of points allowed inside each cut of the form Fig. 10(a) must scale as $L$. Therefore, the number of points covered by the ring scales as $N_R \sim L \times L$, and is an *extensive* property of the system.
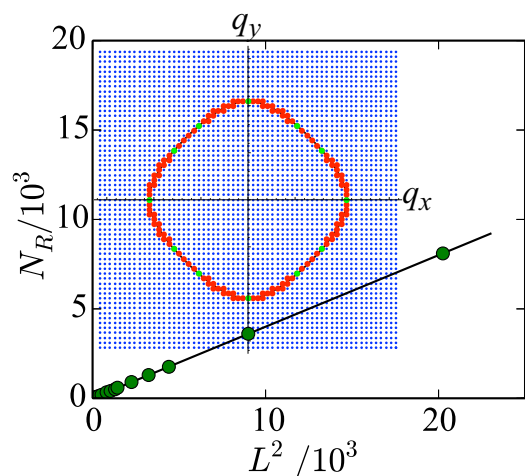


FIG. 11. Evidence that the number of spin configurations contributing to the helicoidal spin liquid, $N_R$, scales linearly with the system size, $N = L^2$. $N_R$ was estimated on the basis of the number of states lying close to the ring defined by [Eq. (20)], for parameters $\mathbf{J}_B$ [Eq. (22)] and system sizes ranging from $L = 12^2$ to $L = 450^2$, as described in Sec. IV A. (Inset) Wave vectors of states contributing to $N_R$ for $L = 60$.
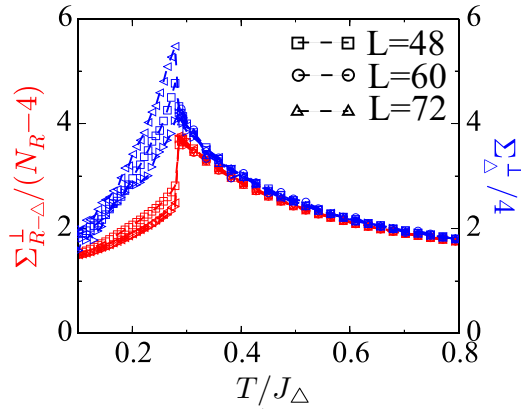
FIG. 12. Comparison between the spectral weight associated with the ordering vectors of the 1/3-magnetization plateau and that associated with the remaining wave vectors belonging to the ring (cf. Fig. 9). The total spectral weight in the ring, $\Sigma_\triangle^\perp$ [Eq. (44)], undergoes a discontinuous drop at the ordering temperature $T = 2.8J_\triangle$, but remains finite in the ordered state. Fluctuations at the ordering vector, $\Sigma_{R-\triangle}^\perp$ [Eq. (46)], are associated with a discontinuous rise at the ordering temperature. Results are taken from classical Monte Carlo simulations of $\mathcal{H}_\square^{\mathrm{FFM}}$ [Eq. (1)] for system sizes $L = 48, 60, 70$, and parameters $\mathbf{J}_B$ [Eq. (22)] with $h = 2.4J_\triangle$.

In order to gain more insight into this state, we define an integral of the transverse structure factor $S^\perp(\mathbf{q})$ [Eq. (35)] over the manifold of states contributing to the ring

$$\Sigma_R^\perp = \sum_{\mathbf{q}} \mathcal{S}^\perp(\mathbf{q}) \quad \forall \; \mathbf{q} \in \{\mathbf{q} | \omega_{\mathrm{1SL}}(\mathbf{q}) < \omega_c\}, \qquad (44)$$

as well as a sum over the discrete wave vectors $Q_\triangle$ [Eq. (36)] associated with three-sublattice order

$$\Sigma_\triangle^\perp = \sum_{\mathbf{q} \in \{Q_\triangle\}} \mathcal{S}^\perp(\mathbf{q}), \qquad (45)$$

and the difference of the two

$$\Sigma_{R-\triangle}^\perp = \Sigma_R^\perp - \Sigma_\triangle^\perp. \qquad (46)$$

Figure 12 shows how these measures of the ring, normalized to the number of contributing wave vectors, evolve across the transition from the high temperature spin liquid into the 1/3-magnetization plateau for $h = 2.4J_\triangle$. It is clear that the $\mathcal{S}(\mathbf{q})$ ring has a uniform height at temperatures away from the phase transition. Right above the transition, enhanced fluctuations in $S^x$-$S^y$ herald three-sublattice order, but the defining characteristics of the ring survive both in the disordered and the ordered limits.

The structure factor per spin,

$$(\Sigma_R/L^2)/N_R \sim \Sigma_R/L^4, \qquad (47)$$

evaluated at a *typical* wave vector $\mathbf{Q}_{\mathrm{ring}}$ [Eq. (20)], is itself not an extensive quantity. Instead, it vanishes as $1/L^2$, as can be seen in Fig. 13(a) for a variety of temperatures in the disordered region. This is also the behavior observed in a standard paramagnetic region. However, the *total* ring structure factor per spin $\Sigma_R/L^2$ is a function of $N_R \sim L^2$ and should therefore be an *extensive* quantity. Figure 13(b) shows that $\Sigma_R/L^2$ converges to a finite value as $L^{-2} \to 0$, and therefore
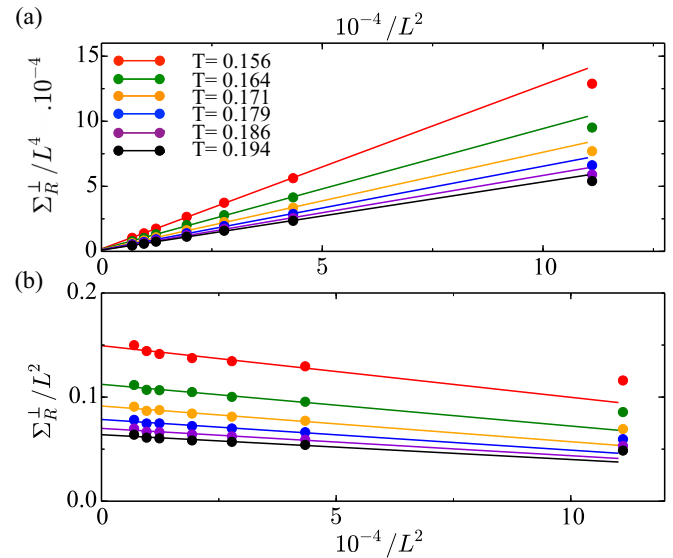


FIG. 13. Evidence for spin-liquid behavior in the finite-size scaling of the integrated structure factor, $\Sigma_R^\perp$ [Eq. (44)]. (a) The total weight associated with spin configurations contributing to the ring vanishes as $1/L^2$ in the thermodynamic limit. (b) The structure factor per spin summed over all ring points, $\Sigma_R^\perp/L^2$, scales linearly with the system size and thus persists in the thermodynamic limit. Lines are a linear fit to the data for the largest system sizes. Results are taken from classical Monte Carlo simulations of $\mathcal{H}_\square^{\mathrm{FFM}}$ [Eq. (1)] for $h = 2.4J_\triangle$ and $T = 0.45J_\triangle$, with exchange parameters $\mathbf{J}_B$ [Eq. (22)].

$\Sigma_R$ is a nonzero quantity in the thermodynamic limit. This is a direct demonstration of an extensive, nontrivial degeneracy in the thermodynamic limit an hallmark of a spin liquid.

### B. Low-temperature conical spiral

We now turn to the nature of the low-temperature ordered state found for $h/J_\triangle \lesssim 1$ and $T/J_\triangle \lesssim 1.7$ in the phase diagram Fig. 8. We find that specific ordered states, with a wave vector belonging to the ring manifold [Eq. (20)], are selected at low temperature. Nonetheless, the ring seen in the spin structure factor $\mathcal{S}(\mathbf{q})$ [Eq. (33)] survives in these ordered phases, as shown in Fig. 12. For magnetic fields $h \gtrsim 1.2J_\triangle$, the magnetization process of the triangular lattice antiferromagnet is recovered, as described in Sec. III for the parameter set $\mathbf{J}_A$ [Eq. (18)]. For values of field $0 \leqslant h \lesssim 1.2J_\triangle$, we observe a strong competition between the coplanar $Y$ state and different conical states, all with uniform magnetization $S_i^z$.

In order to better understand this behavior, we have carried out a low-temperature expansion of the spin-wave excitations around the $T = 0$ classical ground-state manifold, which allows the calculation of corrections to the free energy as a power series in $T$. Details of these calculations are given in Appendix A 1. In the absence of magnetic field, this expansion predicts that low-temperature fluctuations favor a coplanar spiral state described by a single incommensurate wave vector very close to

$$\mathbf{Q}_{1Q} = (\pi/3, \pi/2) \qquad (48)$$

(plus associated mirrors and reflections); cf. Fig 15.

When a small magnetic field is applied, the state favored by fluctuations in the harmonic approach is a *conical*, noncoplanar

FIG. 14. Finite-temperature phase transition between conical-spiral state and magnetic-vortex crystal found for a low value of magnetic field in the phase diagram Fig. 8. (a) Structure factor $\mathcal{S}^\perp(\mathbf{q})$ [Eq. (35)], within the conical-spiral state for $T = 0.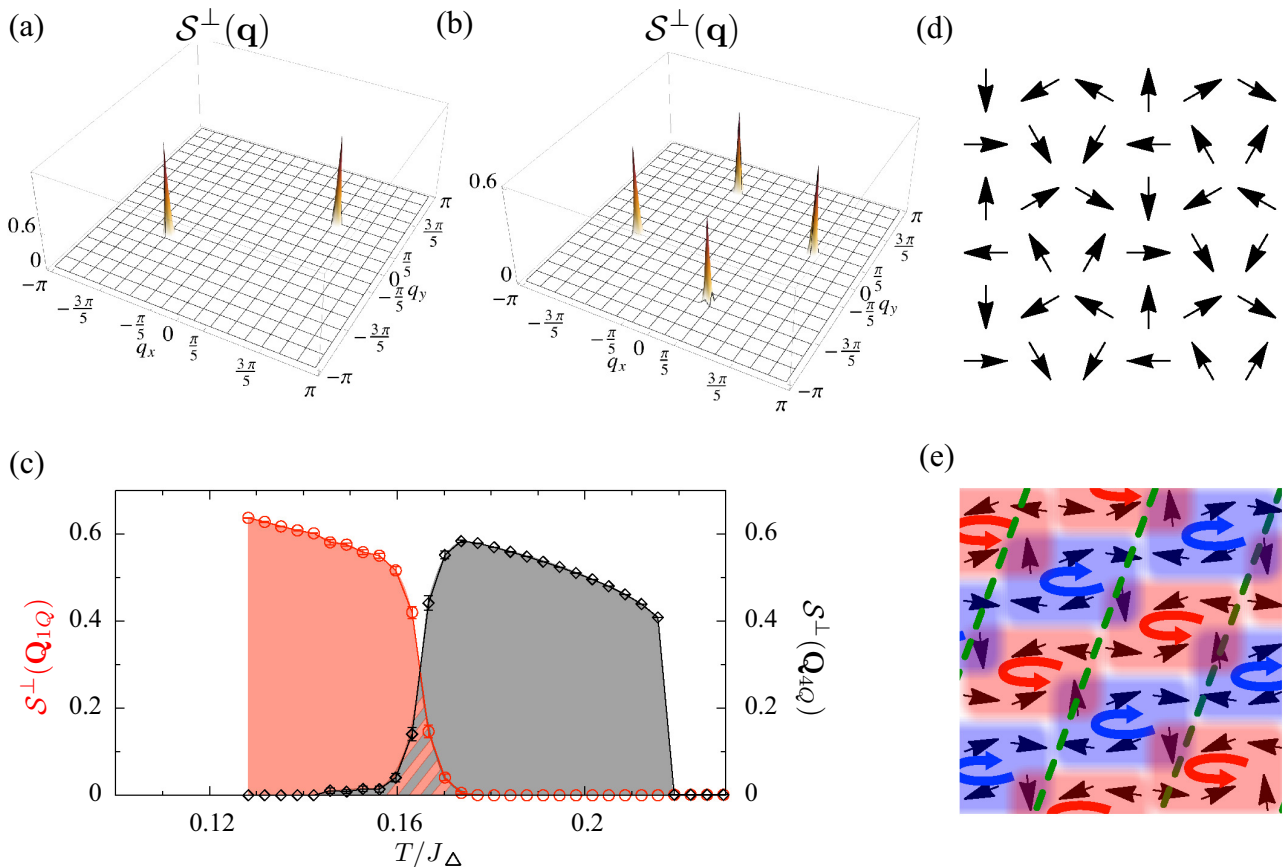13\ J_\triangle$, showing peaks at $\mathbf{Q}_{1Q}$ [Eq. (48)]. (b) Structure factor within the magnetic-vortex crystal for $T = 0.175\ J_\triangle$, showing Bragg peaks at $\mathbf{Q}_{4Q}$ [Eq. (49)]. (c) Temperature dependence of the peaks, showing a phase transition from conical spiral to magnetic-vortex crystal at $T \approx 1.6\ J_\triangle$ (cf. Fig 8). (d) Illustrative spin configuration in the plane perpendicular to magnetic field associated with the $1Q$ conical-spiral state. (e) Illustrative spin configuration in the plane perpendicular to magnetic field associated with the $4Q$ magnetic-vortex crystal. Results for $\mathcal{S}^\perp(\mathbf{q})$ are taken from classical Monte Carlo simulations of $\mathcal{H}_\square^{\mathrm{FFM}}$ [Eq. (1)] for $h = 2.4J_\triangle$, with exchange parameters $\mathbf{J}_B$ [Eq. (22)].

version of the $h = 0$ state; cf. Figs. 14(a) and 14(d). The wave vector of the $h = 0$ spiral is preserved in the $S^x$-$S^y$ plane, while all spins have a constant magnetization along the $S^z$ spin direction. This state has been identified previously as the conical umbrella state in the anisotropic triangular lattice [3,51,72,73]. According to the low-temperature expansion, the entropy of the $Y$ coplanar state increases with increasing value of magnetic field, while that of the conical state decreases. For fields $h \gtrsim 0.8J_\triangle$, the $Y$ state is predicted to be the preferred low-temperature state.

Monte Carlo simulations confirm that, for values of field $0 \leqslant h \lesssim 0.8J_\triangle$, the conical state is stabilized at low temperature, while for $0.8 \lesssim h \leqslant 3J_\triangle$ the $Y$ state is favored. The first-order phase transition between both phases is very difficult to observe in MC simulations, since it happens after *two* other symmetry-breaking phase transitions at higher temperature. We also find, from, e.g., a negative spin stiffness (not shown), that simulations seeded with a conical spin texture with an in-plane wave vector $\mathbf{Q}_{1Q} = (\pi/3, \pi/2)$ show a strong tendency to become slightly incommensurate in the $S^x$-$S^y$ plane, in full agreement with the harmonic approximation. This selection of an incommensurate, noncoplanar phase

by thermal fluctuations is an interesting counterexample to the rule of thumb that fluctuations prefer collinear, or at worst coplanar, phases, as a manifestation of the celebrated order-due-to-disorder effect; cf. [59].

### C. Magnetic vortex crystal

We next consider the nature of the ordered state found for intermediate temperatures, $1.7 < T/J_\triangle \lesssim 2.2$, and low values of magnetic field, $h/J_\triangle \lesssim 1.2$, between the low-temperature conical spiral and the high-temperature spin-liquid phase, as shown in the phase diagram Fig. 8. In this parameter range, Monte Carlo simulations started from a random initial configuration often get trapped in local free-energy minima, resulting in domain walls between different phases. This hints at the presence of competing phases, and a first-order transition, at a lower temperature than the initial ordering transition. Further simulations with open boundary conditions [74] reveal a tendency for the edge spins to be collinear with $S^z$, while the bulk reproduces the same behavior as for periodic boundary conditions. We resort to comparing different parallel-tempering simulations for each value of field,

initialized from a variety of different ordered states, including random configurations, mixing different states in a single replica or across temperature space. This approach does not permit a very accurate location of the phase transition, but gives us confidence on the phases present and on the overall topology of the phase diagram.

Carrying out this analysis, we find a constant-magnetization state with a spin texture in the $S^x$-$S^y$ plane described by *four* wave vectors; cf. Fig. 1(c). Usually, multiple-$Q$ states violate the fixed spin-length constraint $|\mathbf{S}_i| = 1$ and therefore are not favored at low temperatures. However, it is possible to construct a very specific $4Q$ state out of spirals with the wave vector

$$\mathbf{Q}_{4Q} = (3\pi/5, \pi/5) \tag{49}$$

and symmetry-related vectors. For a given magnetization

$$m = S_i^z = \text{const.}, \tag{50}$$

the spin configuration associated with this $4Q$ state is

$$S_i^x = [1 - m^2]^{\frac{1}{2}} \text{Re}[F(\mathbf{r}_i)], \tag{51}$$

$$S_i^y = [1 - m^2]^{\frac{1}{2}} \text{Im}[F(\mathbf{r}_i)], \tag{52}$$

where

$$\begin{aligned} F(\mathbf{r}_i) &= e^{i\mathbf{Q}_A \cdot \mathbf{r}_i} + e^{i2\pi/5} e^{-i\mathbf{Q}_A \cdot \mathbf{r}_i} \\ &\quad + e^{i4\pi/15} e^{i\mathbf{Q}_B \cdot \mathbf{r}_i} + e^{-i8\pi/15} e^{-i\mathbf{Q}_B \cdot \mathbf{r}_i}, \end{aligned} \tag{53}$$

and

$$\begin{aligned} \mathbf{Q}_A &= (\pi/5, -3\pi/5), \\ \mathbf{Q}_B &= (3\pi/5, \pi/5). \end{aligned} \tag{54}$$

For vanishing magnetization ($m = S_i^z \equiv 0$), the $4Q$ state has the form of a lattice of vortices shown in Fig. 14(e). By construction, the $4Q$ state interpolates smoothly to finite magnetization, where it takes on the form illustrated in Fig. 1(c). The associated spin structure factor has four peaks [cf. Fig. 14(b)].

Monte Carlo simulations for a range of fields $0 \lesssim h \lesssim 1.2J_\triangle$, initialized with half of the replicas in the $1Q$ state, and the other half in the $4Q$ state, paint a consistent picture of a double phase transition, as shown in Fig. 14(c), for $h = 0.8J_\triangle$. As the system is cooled down from the paramagnet, a region is found where the $4Q$ state is stabilized, followed by the $1Q$ state at a lower temperature. We conclude that the inner phase transition is probably weakly first order, since we observe no discontinuities in the internal energy, nor any significant release of entropy. Unlike simulations of the $1Q$ state initialized with the $\mathbf{Q}_{1Q} = (\pi/3, \pi/2)$ wave vector, the $4Q$ state does not show a tendency to become incommensurate, which attests to its stability. We observe this scenario of two ordered phases down to the $h = 0$ limit, where both phases lose their conical character by becoming coplanar.

The spin textures of the two noncoplanar states are fundamentally different. A spiral phase described by a single wave vector breaks a reflection symmetry, which can be detected, for example, by defining a chiral order parameter on the $x$

bonds,

$$\kappa_{\text{total}} = \frac{1}{N} \sum_i (\mathbf{S}_i \times \mathbf{S}_{i+\hat{\mathbf{x}}})^z. \tag{55}$$

Conversely, multiple-$Q$ states typically have vanishing net chirality $\langle \kappa_{\text{total}} \rangle = 0$. The $4Q$ state is no exception, and the chirality defined on each plaquette points along the $S^z$ direction but with alternating signs, so that the total chirality is zero. This describes a spin texture where the spin texture winds up in alternating directions across the lattice, which may be visualized as a crystalline structure of alternating magnetic vortices [Fig. 14(e)]. We have not found other possible multiple-$Q$ states with uniform $S^z$ which could be stabilized in this model.

## V. DISCUSSION OF RESULTS

In this article, we have explored some of the novel phases which can arise in a square-lattice frustrated ferromagnet in applied magnetic field. In the process, we have seen a triangular-lattice antiferromagnet reborn on a square lattice, and uncovered a spin liquid and a vortex crystal, both with finite magnetization. In what follows, we examine how these phases compare with known results for frustrated antiferromagnets and sketch some of the possible consequences of quantum fluctuations, previously touched upon in Refs. [46,47].

### A. Three-sublattice physics and 1/3-magnetization plateau

The phase diagram for the square-lattice frustrated ferromagnet $\mathcal{H}_\square^{\text{FFM}}$ [Eq. (1)] for the parameter set $\mathbf{J}_A$ [Eq. (18)], shown in Fig. 2, is markedly different from what might normally be expected in a square-lattice frustrated magnet [75]. However, it is remarkably similar to that of the triangular-lattice antiferromagnet, developed in [23]. This similarity extends beyond the phases found—canted $Y$ state, collinear 1/3-magnetization plateau, and 2:1 canted phase—and the topology of the resulting phase diagram, into the finite-size scaling of the associated phase transitions (compare Figs. 2 and 5 of this article with Figs. 1 and 2 of [23]).

These results are striking, since the collinear 1/3-magnetization plateau is usually thought to be a hallmark of triangular-lattice physics, stabilized by a delicate order-by-disorder effect [6,59,60]. Here, however, a robust 1/3-magnetization plateau, with three-sublattice order, arises in a model more naturally associated with incommensurate phases. In fact, for this particular parameter set, the only significant difference between the square-lattice and triangular-lattice models is the way in which ordered phases break lattice-rotation symmetry.

Given the degree of fine tuning in the choice of parameters, it is natural to ask what happens when $\mathcal{H}_\square^{\text{FFM}}$ [Eq. (1)] is tuned away from the special line $J_3 = J_2 - |J_1|/2$ (cf. Fig. 4). In this case, the collinear and coplanar phases of Fig. 2 would no longer belong to the $T = 0$ ground-state manifold. However, commensurate, collinear phases with $\mathbf{Q} = (\frac{2\pi}{3}, 0)$ or $(0, \frac{2\pi}{3})$ are still generically more favored by thermal fluctuations than noncollinear or noncoplanar phases [59]. In the case of the Heisenberg antiferromagnet on an anisotropic triangular

lattice, it is known that quantum fluctuations can stabilize a 1/3-magnetization plateau, even where it is not a classical ground state [57,73,76].

In the present case, our preliminary Monte Carlo simulations hint at a rich phase diagram near the line $J_3 = J_2 - |J_1|/2$. At the lowest temperatures, conical phases with incommensurate wave vector predominate. However, at higher temperatures, commensurate, coplanar phases, and, in particular, the collinear 1/3-magnetization plateau, are restored by fluctuations [74]. The full determination of the corresponding phase diagram remains an open problem and may require use of an algorithm specially adapted to incommensurability [77].

Another question of obvious interest is what happens for quantum spins. For large $S$, it seems reasonable to expect that quantum fluctuations would act much like thermal fluctuations, stabilizing triangular-lattice physics in the square-lattice frustrated ferromagnet, both on the special line $J_3 = J_2 - |J_1|/2$ and near it. The extreme quantum limit of $\mathcal{H}_\square^{\text{FFM}}$ [Eq. (1)], for spin $S = 1/2$, has already been studied in exact diagonalization [46]. These studies confirm the existence of 1/3-magnetization plateau at $T = 0$, for intermediate values of magnetic field, and a range of parameters close to the line $J_3 = J_2 - |J_1|/2$. However, at higher values of field, instead of interpolating to saturation through a canted phase, the magnetization plateau gives way to a quantum spin-nematic phase (cf. [9,47]).

It is also reasonable to ask what phases arise for other parameter sets where the classical ground state of $\mathcal{H}_\square^{\text{FFM}}$ [Eq. (1)] is commensurate with the lattice. These will occur on lines

$$J_1 + 2J_2 + 4J_3 \cos\left(\frac{2\pi}{p}\right) = 0, \qquad (56)$$

for all integer $p > 3$, with associated ordering vector

$$\mathbf{Q}_p = \left(\frac{2\pi}{p}, 0\right). \qquad (57)$$

The parameter set $\mathbf{J}_A$ [Eq. (18)], with three-sublattice order, corresponds to $p = 3$.

Our preliminary investigation of this question, using classical Monte Carlo simulation [74] and exact diagonalization [46], suggests that the answer is not simple. For $p = 4$, we do indeed find four-sublattice order. However, thermal fluctuations favor a collinear state with "up-up-down-down" stripe order over the expected 1D spiral. This collinear state cants in applied magnetic field in a way reminiscent of the planar ($XY$) model [78]. Quantum fluctuations select the same, collinear, stripe order for $p = 4$ [46]. Meanwhile, exact diagonalization carried out for $\mathbf{J} = (-1, 0.3, 0.175)$, i.e., $p = 6$, for clusters of up to $N = 36$ spins, indicate that the ground state *is* a commensurate 1D spiral. They also suggest the possibility of a 1/3-magnetization plateau in applied magnetic field. Clearly, this issue merits further investigation.

### B. Spin-liquid and ring correlations

The phase diagram shown in Fig. 8, calculated for the parameter set $\mathbf{J}_B$, where different spiral phases meet, looks superficially similar to the one for the parameter set associated with three-sublattice order $\mathbf{J}_A$, shown in Fig. 2. However, the addition of a degenerate manifold of classical ground states leads to a number of crucial differences, especially at high temperature, and for low values of magnetic field.

The most obvious consequence of the enlarged ground-state manifold is the ring seen in the structure factor, as shown in Fig. 9. This ring is present in both the low-temperature ordered phases and the high-temperature paramagnet for all values of magnetic field. Simulations for more generic parameter sets [74] confirm that this ring is a generic feature of the classical phase boundary between 1D and 2D spiral ground states (cf. Fig. 4).

At finite temperature, the number of low-lying states contributing to the ring in the structure factor, $\Sigma_R$ [Eq. (44)], scales with the size of the system (Figs. 10 and 11). As a consequence, the ring makes a macroscopic contribution to the entropy of the system, even though the number of classical ground states, defined by Eq. (20), scales only with the linear dimension of the system $L$. The high-temperature paramagnet phase in Fig. 8 can therefore be viewed as a spin liquid with a finite magnetization.

The spin liquid found in this two-dimensional frustrated ferromagnet differs from well-known three-dimensional examples, such as spin ice [79], or the pyrochlore Heisenberg antiferromagnet [80] in that the classical ground-state manifold is subextensive. It has more in common with problems where the ground-state manifold correspond to lines or surfaces in reciprocal space, such as the chiral spin liquid found on the diamond lattice [81], or the ring and "pancake" liquids reported in the frustrated honeycomb antiferromagnet [48]. We note, however, that, unlike the honeycomb lattice example, we do not find any crossover to a conventional paramagnet at high temperatures.

In the absence of a more complete description, we refer to the new state as a "helicoidal" spin liquid, in recognition of the fact that the system displays short-range helicoidal correlations [82]; cf. Fig. 10. The better characterization of this phase remains an open problem.

### C. Conical spiral

Besides supporting a spin liquid, the ground-state manifold for the parameter set $\mathbf{J}_B$ [Eq. (22)] has the special property that it contains a large number of simple, commensurate wave vectors, $\mathbf{Q}_R$ [Eq. (42)]. This sets the stage for a rather unusual form of order-by-disorder, in which both single-$Q$ and multiple-$Q$ ordered states are selected by fluctuations from states belonging to the ring of allowed $\mathbf{Q}$ (cf. Fig. 9). Both of these phases are present for $h = 0$ and persist for a finite range of magnetic field, as shown in Fig. 8.

At the lowest temperatures, thermal fluctuations select an incommensurate single-$Q$ state with the character of conical spiral, familiar from studies of the Heisenberg antiferromagnet on an anisotropic triangular lattice [3,51,72,73]. This spiral has uniform magnetization $S^z$ and wave vector very close to $\mathbf{Q}_{1Q}$ [Eq. (48)]. In the limit $T \to 0$, we can use a low-temperature expansion to show that this incommensurate spiral makes a larger contribution to entropy than any other state in the ground-state manifold of the model (cf. Appendix B). The same state is found in classical Monte Carlo simulations at low temperatures $T \lesssim 0.17 J_\Delta$ and low values of magnetic field

$h \lesssim J_\Delta$; cf. Fig. 8. At low temperatures, but larger values of magnetic field, this incommensurate non–coplanar state gives way to the commensurate, coplanar $Y$ state familiar from the triangular-lattice antiferromagnet (cf. Fig. 8 with Fig. 1 of Ref. [62]).

It is a widely quoted "rule of thumb" that fluctuations in frustrated magnets, whether quantum or classical, favor coplanar—and, if possible, collinear—states [59]. It is also frequently assumed (without proof) that quantum and thermal fluctuations will favor the same state. The present case provides an interesting counterexample. Somewhat surprisingly, thermal fluctuations select an incommensurate spiral for $T \to 0$, as discussed above. Meanwhile, as shown in Appendix D, quantum fluctuations, treated at the level of linear spin-wave theory, prefer a state with commensurate wave vector $\mathbf{Q}_{3\mathrm{sub}}^{1\mathrm{D}}$ [Eq. (11)].

By analogy with the quantum Heisenberg antiferromagnet on a triangular lattice [60], we anticipate that the resulting quantum ground state will support three-sublattice, coplanar, $120°$ order for $h = 0$, giving way to a coplanar $Y$ state in applied magnetic field. Thus, for low values of magnetic field, quantum and thermal effects compete, setting up the possibility of a phase transition from the commensurate quantum ground state into the incommensurate state favored by thermal fluctuations, as temperature is increased. In practice, this would mean that the coplanar $Y$ state, already favored by thermal fluctuations for larger value of field—cf. Fig. 8— would displace the conical spiral for $T \to 0$.

### D. Vortex crystal

While the conical spiral is a relatively conventional phase, the structure of the vortex crystal marks it out as very different from anything found in triangular-lattice Heisenberg antiferromagnets. The vortex crystal is formed through the coherent superposition of classical ground states with four, symmetry-related wave vectors [Fig. 14(b)]. It is not selected by harmonic thermal fluctuations (cf. Appendix C), but rather by anharmonic (interaction) effects which become important at higher temperatures. At a more intuitive level, this $4Q$ state can be visualized as a lattice of vortices in $S^x$-$S^y$ plane, with alternating vector chirality [Fig. 1(c)]. The resulting "crystal" has a ten-site unit cell [cf. Fig. 14(e)] and meets the usual definition of a magnetic supersolid, since it spontaneously breaks the translational symmetry of the lattice, while at the same time breaking spin-rotation symmetry about the direction of the magnetic field (cf. Refs. [7,62] and references therein). However, it differs from other examples of magnetic supersolids, in that it has a uniform magnetization $S^z$, and translational symmetry is instead broken by the spin texture perpendicular to magnetic field.

Crystals formed of vortices have been widely studied in the context of type II superconductors, where they are known as a "vortex lattice" [54,55]. Lattices of magnetic vortices are, however, very unusual, recent work on Mott insulators notwithstanding [52]. The $4Q$ state, described above, is not an exact analog of a superconducting vortex lattice, since it contains vortices with alternating circulation. Nonetheless, it is an interesting step in that direction. The vortex crystal also proves to be a robust state; we have checked in simulation that it

survives for deviations in exchange parameters $\delta\mathbf{J} \approx 0.01|J_1|$. This robustness reflects the fact that it is only possible to form a $4Q$ state from classical ground states specific to the parameter set $\mathbf{J}_B$, ruling out any continuous transformation into an incommensurate state.

Recently, more attention has been paid to a different kind of crystals of topological defects: lattice states of Skyrmions [11,12,51,83]. In a Skyrmion lattice the spin texture also also winds in alternating directions, but the core of each Skyrmion is associated with a modulated $S^z$. In fact, modulation along the $S^z$ direction seems to be a generic feature of multiple-$Q$ states found in magnetic models [50,51]. This is a strong constraint and might account for the lack of other examples of vortex crystals in spin models. In light of the recent work on Skyrmion lattices, it might also be interesting to explore how a vortex crystal couples to itinerant electrons.

It would also be of value to investigate how the $1Q$ and $4Q$ states found in classical simulations of $\mathcal{H}_\square^{\mathrm{FFM}}$ evolve in the presence of quantum fluctuations. On general grounds, we anticipate that the phases shown in Fig. 8 should survive for large (quantum) spin. In principle, this could be investigated by self-consistent mean-field methods. The picture for spin-$\frac{1}{2}$ is, however, harder to assess. Exact diagonalization studies reveal a very rich ground-state phase diagram in the absence of magnetic field and suggest a disordered ground state for the parameter set $\mathbf{J}_B$ (Refs. [46,47]). However, given the small cluster sizes available, and the large unit cell of the $4Q$ state, it is impossible to rule out a vortex crystal ground state for spin $S = 1/2$.

### VI. CONCLUSIONS

In this article we have explored some of the novel phases which arise in a simple model of a two-dimensional frustrated ferromagnet; the $J_1$-$J_2$-$J_3$ Heisenberg model on a square lattice, $\mathcal{H}_\square^{\mathrm{FFM}}$ [Eq. (1)]. We have chosen to concentrate on the effect of thermal, rather than quantum fluctuations, using large-scale classical Monte Carlo simulation, complemented by linear spin-wave theory, to determine the finite-temperature phase diagram of the model in applied magnetic field.

Two distinct parameter sets were considered. The first of these, $\mathbf{J}_A$ [Eq. (18)], was chosen in order to favor three-sublattice stripe order. In this case we find a phase diagram, Fig. 2, remarkably similar to that of the Heisenberg antiferromagnet on a triangular lattice [23]. In applied magnetic field, a $120°$ ground state transforms first into a canted $Y$ state and then into a collinear $1/3$-magnetization plateau, illustrated in Fig. 1(c), before interpolating through a 2:1 canted phase to saturation.

The second parameter set, $\mathbf{J}_B$ [Eq. (22)], was chosen to lie at the classical phase boundary between one-dimensional and two-dimensional spiral ground states. Here an enlarged ground-state manifold manifests itself in a ring structure in the spin structure factor [Fig. 1(b)] and in a much richer phase diagram (Fig. 8). In this case, the phases found include a high-temperature spin liquid and a number of new ordered phases, as well as the $Y$-state, $1/3$-magnetization plateau and 2:1 canted phase familiar from the Heisenberg antiferromagnet on a triangular lattice. In particular, for low values of magnetic field, a multiple-$Q$ state with the character of a vortex crystal

[Fig. 1(c)] competes with an incommensurate conical-spiral state. These results are quite striking, and the subtle play of order by disorder which drives the finite-temperature phase transition between the incommensurate conical spiral and vortex crystal states would have been very difficult to anticipate *a priori*.

The abundance of exotic phases found in this simple model suggests that there is much still to learn about frustrated ferromagnets. In particular, questions of commensurability, and of the role of quantum fluctuations, deserve further investigation. With respect to commensurability, an obvious open question is whether vortex crystals, like the one studied in this article, can form different lattices, or lattices with different lattice constants. Quantum effects are expected to lead to an even richer phenomenology, stabilizing new forms of magnetic order, as well as valence bond solid and spin-nematic states, with exact diagonalization hinting at the possibility of a spin-liquid ground state [46]. Also, while the square-lattice Heisenberg model $\mathcal{H}_\square^{\mathrm{FFM}}$ provides a simple context for these questions, we anticipate that the same effects may be observed in a much wider range of systems.

We conclude with a few comments on experiment. A number of magnetic insulators have been proposed as examples of square-lattice frustrated ferromagnets. These include the vanadium phosphates $Pb_2VO(PO_4)_2$ [16], $BaCdVO(PO_4)_2$ [17], and $SrZnVO(PO_4)_2$ [18] and the copper-based topotactic ion-exchange systems $(CuCl)LaNb_2O_7$ [19], $(CuBr)Sr_2Nb_3O_{10}$, [20], and $(CuBr)Sr_2Nb_3O_{10}$ [21]. The properties of the vanadium phosphates in applied magnetic field appear to be well described by a simple $J_1$-$J_2$ model [38,39]. However, the much richer phenomenology of the cuprates suggests more complicated exchange interactions, which need not have the full symmetry of the square lattice [22].

In the absence of a clear experimental validation from, e.g., inelastic neutron scattering, the Hamiltonian $\mathcal{H}_\square^{\mathrm{FFM}}$ [Eq. (1)] is probably best regarded as a toy model capturing some of the the interesting features of quasi-two-dimensional frustrated ferromagnets, rather than a complete description of the exchange interactions in these layered cuprates. Nonetheless, this model does score two notable successes, in providing a route to both the 1/3-magnetization plateau observed $(CuBr)Sr_2Nb_3O_{10}$ [20] and the helical order found in $(CuBr)Sr_2Nb_3O_{10}$ [21]. In the light of this, it would be very interesting to see further experiments on square-lattice frustrated ferromagnets in applied magnetic field.

### APPENDIX A: LOW-TEMPERATURE ENTROPY IN THE HARMONIC APPROXIMATION AND ITS RELATION TO SPIN-WAVE THEORY

In this appendix we provide details of the spin-wave calculations used to explore the different ordered phases selected by fluctuations. We start by reviewing the low-temperature expansion of classical spin model and show how it can be used to explicitly calculate the free energy, and thereby the entropy, associated with a given form of magnetic order, to leading order in $T$ (Sec. 1 of this Appendix). We then show how equivalent results for the free energy can be obtained from the spin-wave dispersion obtained within linear spin-wave theory for the associated quantum model, using the conical-spiral state as a worked example (Sec. 2 of this Appendix).

Finally, we derive explicit expressions for the entropy associated with the different forms of magnetic order encountered in this work: (i) conical spirals in applied magnetic field (Sec. 3 of this Appendix ), (ii) coplanar $K$-sublattice states with in-plane magnetic field, such as the $Y$ state (Sec. 4 of this Appendix), (iii) canted conical $K$-sublattice states such as the $4Q$ state in applied field (Sec. 5 of this Appendix).

#### 1. Entropy within a classical low-temperature expansion

The low-temperature thermodynamics of a classical spin model of the form Eq. (1) can be calculated through an expansion of the Hamiltonian in small fluctuations about the ground-state ($T = 0$) configuration. For this purpose, one may proceed as follows. Let us consider a magnetic ground state with $K$ sublattices. Without loss of generality, it is possible to select a reference frame such that, in this ground state, the spin on the $\nu$th sublattice ($\nu = 1, \ldots, K$) in the $m$th unit cell at position $\mathbf{R}_{\nu,m}$ is written as

$$\mathbf{S}_{\nu,m}^0 = \begin{bmatrix} S_{\nu,m}^x \\ S_{\nu,m}^y \\ S_{\nu,m}^z \end{bmatrix} = \begin{bmatrix} \sin(\theta_{\nu,m})\sin(\phi_{\nu,m}) \\ \cos(\theta_{\nu,m}) \\ \sin(\theta_{\nu,m})\cos(\phi_{\nu,m}) \end{bmatrix}. \quad \text{(A1)}$$

We then choose for each site ($\nu,m$) a local frame $(\tilde{\mathbf{e}}_x, \tilde{\mathbf{e}}_y, \tilde{\mathbf{e}}_z)$, rotated from the reference frame, such that $\tilde{\mathbf{e}}_z$ coincides with the ground-state spin direction $\mathbf{S}_{\nu,m}^0$, and expand the spin components in this frame as

$$\mathbf{S}_{\nu,m} = \begin{bmatrix} x_{\nu,m} \\ y_{\nu,m} \\ z_{\nu,m} \approx 1 - \frac{x_{\nu,m}^2 + y_{\nu,m}^2}{2} \end{bmatrix}, \quad \text{(A2)}$$

where $x_{\nu,m}$ and $y_{\nu,m}$ denote transverse components of a spin deviation. One has, in the harmonic approximation,

$$\mathcal{H} = \mathcal{H}^{(0)} + \mathcal{H}^{(2)}, \quad \text{(A3)}$$

where $\mathcal{H}^{(0)}$ is the energy of the ground state and $\mathcal{H}^{(2)}$ is quadratic in spin deviations. For $N$ spins with $N_c$ unit cells ($N_c = N/K$),

$$\mathcal{H}^{(2)} = \tfrac{1}{2}\hat{\xi}^T \mathcal{M}\hat{\xi}, \quad \text{(A4)}$$

where $\hat{\xi}$ is a $2N$-dimensional vector of spin deviations,

$$\hat{\xi}^T = [x_{1,1}, \ldots, x_{K,Nc}, y_{1,1}, \ldots, y_{K,Nc}], \quad \text{(A5)}$$

and $\mathcal{M}$ a symmetric $2N \times 2N$ matrix. By Fourier transforming the spin deviations

$$x(y)_{\nu,m} = \frac{1}{\sqrt{N_c}} \sum_{\mathbf{k}} x(y)_{\nu,\mathbf{k}} e^{i\mathbf{k}\cdot\mathbf{R}_{\nu,m}}, \qquad (A6)$$

Eq. (A4) becomes

$$\mathcal{H}^{(2)} = \frac{1}{2} \sum_{\mathbf{k}\in M_{\mathrm{BZ}}} \hat{\xi}_{-\mathbf{k}}^T \mathcal{M}(\mathbf{k})\hat{\xi}_{\mathbf{k}} \qquad (A7)$$

where

$$\hat{\xi}_{\mathbf{k}}^T = [x_{1,\mathbf{k}}, \ldots, x_{K,\mathbf{k}}, y_{1,\mathbf{k}}, \ldots, y_{K,\mathbf{k}}]. \qquad (A8)$$

Here $M_{\mathrm{BZ}}$ denotes the magnetic Brillouin zone for the $K$-sublattice structure, and $\mathcal{M}(\mathbf{k})$ is a $2K \times 2K$ Hermitian matrix. Diagonalizing $\mathcal{M}(\mathbf{k})$ by a unitary transformation, one obtains the form

$$\mathcal{H}^{(2)} = \frac{1}{2} \sum_{\nu}^{2K} \sum_{\mathbf{k}\in M_{\mathrm{BZ}}} \kappa_{\nu,\mathbf{k}} \zeta_{\nu,\mathbf{k}} \zeta_{\nu,-\mathbf{k}}, \qquad (A9)$$

where $\kappa_{\nu,\mathbf{k}}$ are the eigenvalues of $\mathcal{M}(\mathbf{k})$. The free energy per site at low $T$ is written as

$$\frac{\mathcal{F}}{N} = \frac{E_0}{N} - T \ln T - T \frac{S_{sw}}{N} + \mathcal{O}(T^2), \qquad (A10)$$

where

$$\frac{S_{sw}}{N} = -\langle \ln \kappa_{\nu,\mathbf{k}} \rangle = -\frac{1}{2N} \sum_{\nu=1}^{2K} \sum_{\mathbf{k}} \ln \kappa_{\nu,\mathbf{k}}, \qquad (A11)$$

is the entropy per spin associated with harmonic spin fluctuations [84]. We note that the evaluation of $\langle \ln \kappa_{\nu,\mathbf{k}} \rangle$ does not require the computation of the eigenvalues of $\mathcal{M}(\mathbf{k})$ but only of its determinant $|\mathcal{M}(\mathbf{k})|$, since

$$\langle \ln \kappa_{\nu,\mathbf{k}} \rangle = \frac{1}{2N} \sum_{\mathbf{k}} \ln \left[ \prod_{\nu}^{2K} \kappa_{\nu,\mathbf{k}} \right]$$

$$= \frac{1}{2N} \sum_{\mathbf{k}} \ln |\mathcal{M}(\mathbf{k})|. \qquad (A12)$$

### 2. Alternative derivation of entropy from linear spin-wave theory for a quantum model

It is also possible to evaluate the determinant $|\mathcal{M}(\mathbf{k})|$ [Eq. (A12)], which determines the low-temperature entropy of classical spins [Eq. (A11)], starting from a linear spin-wave (LSW) theory for quantum spins. To show how this works, we first derive the large-$S$, LSW expansion of $\mathcal{H}_{\square}^{\mathrm{FFM}}$ [cf. Eq (1)] and then take a classical limit, setting $S = 1$.

We consider the same ground-state configuration with $K$ sublattices as discussed in Sec. 1 of this Appendix. After the rotation to the local frames and a Holstein-Primakoff transformation of spin operators into bosonic creation and annihilation operators $a_{\nu,\mathbf{k}}^\dagger$ and $a_{\nu,\mathbf{k}}$,

$$\mathbf{S}_{\nu,m} \approx \begin{bmatrix} \sqrt{S/2}(a_{\nu,m} + a_{\nu,m}^\dagger) \\ -i\sqrt{S/2}(a_{\nu,m} - a_{\nu,m}^\dagger) \\ S - a_{\nu,m}^\dagger a_{\nu,m} \end{bmatrix}, \qquad (A13)$$

the harmonic Hamiltonian for spin $S$ is written in the form

$$\mathcal{H}_{\mathrm{qu}}^{(2)} = \frac{1}{2} \sum_{\mathbf{k}} [\hat{\mathbf{a}}_{\mathbf{k}}^\dagger M(\mathbf{k})\hat{\mathbf{a}}_{\mathbf{k}} - \Delta_{\mathbf{k}}], \qquad (A14)$$

where

$$\hat{\mathbf{a}}_{\mathbf{k}}^\dagger = [a_{1,\mathbf{k}}^\dagger \ldots, a_{K,\mathbf{k}}^\dagger, a_{1,-\mathbf{k}}, \ldots, a_{K,-\mathbf{k}}], \qquad (A15)$$

$M(\mathbf{k})$ denotes a $2K \times 2K$ matrix, and $\Delta_{\mathbf{k}}$ is a scalar function which determines the zero-point energy associated with a given form of order.

We can diagonalize $\mathcal{H}_{\mathrm{qu}}^{(2)}$ [Eq. (A14)] using a (paraunitary) Bogoliubov transformation [85]

$$\hat{\mathbf{a}}_{\mathbf{k}} = T_{\mathbf{k}}\hat{\mathbf{b}}_{\mathbf{k}}, \qquad (A16)$$

such that

$$T_{\mathbf{k}}^\dagger I_{-1} T_{\mathbf{k}} = I_{-1}, \qquad (A17)$$

with

$$I_{-1} = \begin{bmatrix} I_K & 0 \\ 0 & -I_K \end{bmatrix}, \qquad (A18)$$

and a $K \times K$ identity matrix $I_K$, brings $\mathcal{H}^{(2)}$ into a diagonal form,

$$\mathcal{H}_{\mathrm{qu}}^{(2)} = \frac{1}{2} \sum_{\mathbf{k}} [\hat{\mathbf{b}}_{\mathbf{k}}^\dagger \Omega(\mathbf{k})\hat{\mathbf{b}}_{\mathbf{k}} - \Delta_{\mathbf{k}}], \qquad (A19)$$

with

$$\Omega(\mathbf{k}) = I_{-1} T_{\mathbf{k}}^{-1} I_{-1} M(\mathbf{k}) T_{\mathbf{k}} = \begin{bmatrix} \omega_{\mathbf{k}} & 0 \\ 0 & \omega_{-\mathbf{k}} \end{bmatrix}, \qquad (A20)$$

where $\tilde{\omega}_{\mathbf{k}}$ is the diagonal matrix

$$\tilde{\omega}_{\mathbf{k}} = \begin{bmatrix} \omega_{1,\mathbf{k}} & & & 0 \\ & \omega_{2,\mathbf{k}} & & \\ & & \ddots & \\ 0 & & & \omega_{K,\mathbf{k}} \end{bmatrix} \qquad (A21)$$

and $\omega_{\nu,\mathbf{k}}$ is the spin-wave frequency in the $\nu$ branch at wave vector $\mathbf{k}$.

We now consider a classical limit in Eq. (A14) by setting $S = 1$ in order to compare it with the classical harmonic Hamiltonian Eq. (A4). In the classical limit the spin operators $a_{\nu,\mathbf{k}}$ and $a_{\nu,\mathbf{k}}^\dagger$ are replaced with complex conjugate scalar fields $\psi_{\nu,\mathbf{k}}$ and $\psi_{\nu,-\mathbf{k}}^*$. (This corresponds to considering a path integral formulation and omitting the imaginary-time dependence in the fields.) In this classical limit, the Holstein-Primakoff transformation Eq. (A13) of $S = 1$ spins in the lowest order becomes equivalent to the expansion Eq. (A2) of classical spins, if we set

$$\psi_{\nu,\mathbf{k}} = (x_{\nu,\mathbf{k}} + iy_{\nu,\mathbf{k}})/\sqrt{2},$$
$$\psi_{\nu,-\mathbf{k}}^* = (x_{\nu,-\mathbf{k}} - iy_{\nu,-\mathbf{k}})/\sqrt{2}. \qquad (A22)$$

Thus, the classical limit of the quantum $S = 1$ harmonic Hamiltonian becomes equivalent to the classical harmonic Hamiltonian under the transformation

$$\hat{\psi}_{\mathbf{k}} = \mathcal{T}\hat{\xi}_{\mathbf{k}}, \qquad (A23)$$

with

$$\hat{\psi}_{\mathbf{k}}^T = [\psi_{1,\mathbf{k}}^*, \ldots, \psi_{K,\mathbf{k}}^*, \psi_{1,\mathbf{k}}, \ldots, \psi_{K,\mathbf{k}}], \quad \text{(A24)}$$

and

$$\mathcal{T} = \frac{1}{\sqrt{2}} \begin{bmatrix} 1 & & & 0 & -i & & & 0 \\ & 1 & & & & -i & & \\ & & \ddots & & & & \ddots & \\ 0 & & & 1 & 0 & & & -i \\ 1 & & & 0 & i & & & 0 \\ & 1 & & & & i & & \\ & & \ddots & & & & \ddots & \\ 0 & & & 1 & 0 & & & i \end{bmatrix}. \quad \text{(A25)}$$

Since $\Delta_{\mathbf{k}}$ originates from commutation relations of operators, it can be neglected in the classical limit. Comparing both classical Hamiltonians, one finds that

$$\hat{\xi}_{-\mathbf{k}}^T \mathcal{M}(\mathbf{k}) \hat{\xi}_{\mathbf{k}} = \hat{\psi}_{-\mathbf{k}}^T M(\mathbf{k}) \hat{\psi}_{\mathbf{k}}, \quad \text{(A26)}$$

which entails

$$\mathcal{M}(\mathbf{k}) = \mathcal{T}^\dagger M(\mathbf{k}) \mathcal{T}. \quad \text{(A27)}$$

From this relation one immediately obtains

$$|\mathcal{M}(\mathbf{k})| = |M(\mathbf{k})|, \quad \text{(A28)}$$

since $|\mathcal{T}^\dagger||\mathcal{T}| = 1$, and from Eq. (A20)

$$|M(\mathbf{k})| = |\Omega(\mathbf{k})| = \prod_{\nu}^{K} \omega_{\nu,\mathbf{k}} \omega_{\nu,-\mathbf{k}}. \quad \text{(A29)}$$

Setting $S = 1$, we obtain the relation

$$|\mathcal{M}(\mathbf{k})| = \prod_{\nu}^{K} \omega_{\nu,\mathbf{k}} \omega_{\nu,-\mathbf{k}}. \quad \text{(A30)}$$

With this result in place, the entropy $S_{sw}$ entering into the classical free energy $\mathcal{F}$ [Eq. (A10)] can be calculated from the linear, quantum spin-wave dispersion $\omega_{\nu,\mathbf{k}}$ [Eq. (A21)] through

$$\frac{S_{sw}}{N} = -\langle \ln \kappa_{\mathbf{k}} \rangle = \frac{1}{2N} \sum_{\mathbf{k}} \ln |\mathcal{M}(\mathbf{k})|$$

$$= -\frac{1}{N} \sum_{\nu=1}^{K} \sum_{\mathbf{k}} \ln \omega_{\nu,\mathbf{k}} = -\langle \ln \omega_{\nu \mathbf{k}} \rangle. \quad \text{(A31)}$$

We explicitly show in the next section that Eq. (A30) holds for spiral states. We note that the spin-wave frequencies $\omega_{\nu,\mathbf{k}}$ could also be obtained by solving the semiclassical equations of motion for the quantum spin-1 model.

In conclusion, the classical entropy per spin, $S_{sw}/N$, can be calculated from either the determinant of the matrix $\mathcal{M}(\mathbf{k})$ [Eq. (A12)] found within a classical low-temperature expansion or the values of the dispersion $\omega_{\nu,\mathbf{k}}$ obtained within LSW theory [Eq. (A21)]. The first approach is slightly simpler but the latter is also interesting as it provides information on the dynamics for both the classical and the quantum model in the semiclassical approximation. It may also be more rapidly implemented if the LSW theory of the model has been derived previously.

### 3. Conical spirals

For the case of conical spirals, it is convenient to choose the reference frame such that the magnetic field $\mathbf{h}$ is along the $S^y$ axis, instead of the $S^z$ axis. The ground-state spins of the conical spirals have then the same projection on the $S^y$ axis, whereas their projections on the $S^x$-$S^z$ plane describe a spiral with wave vector $\mathbf{Q}$. So, they can be written as in Eq. (A1), with equal $\theta$ for all sites, introducing just one sublattice ($K = 1$) as $\phi_{1,m} = \phi_m = \mathbf{Q} \cdot \mathbf{R}_m$, where $\mathbf{R}_m$ is the location of the site $m$. After the rotation to the local frames $(\tilde{\mathbf{e}}_x, \tilde{\mathbf{e}}_y, \tilde{\mathbf{e}}_z)$ and the expansion in spin deviations, the harmonic Hamiltonian reads

$$\mathcal{H}^{(2)} = \frac{1}{2} \sum_{\mathbf{k}} \hat{\xi}_{-\mathbf{k}}^T \mathcal{M}(\mathbf{k}) \hat{\xi}_{\mathbf{k}}$$

$$= \frac{1}{2} \sum_{\mathbf{k}} [x_{-\mathbf{k}}, y_{-\mathbf{k}}] \begin{bmatrix} \mathcal{M}^{xx}(\mathbf{k}) & \mathcal{M}^{xy}(\mathbf{k}) \\ \mathcal{M}^{yx}(\mathbf{k}) & \mathcal{M}^{yy}(\mathbf{k}) \end{bmatrix} \begin{bmatrix} x_{\mathbf{k}} \\ y_{\mathbf{k}} \end{bmatrix}. \quad \text{(A32)}$$

Here $\mathcal{M}(\mathbf{k})$ is the $2 \times 2$ Hermitian matrix with coefficients

$$\mathcal{M}^{xx}(\mathbf{k}) = \frac{1}{2}[J(\mathbf{k}+\mathbf{Q}) + J(\mathbf{k}-\mathbf{Q})] - J(\mathbf{Q}),$$

$$\mathcal{M}^{yy}(\mathbf{k}) = \mathcal{M}^{xx}(\mathbf{k})\cos^2\theta + [J(\mathbf{k}) - J(\mathbf{Q})]\sin^2\theta, \quad \text{(A33)}$$

$$\mathcal{M}^{xy}(\mathbf{k}) = [M^{yx}(\mathbf{k})]^* = \frac{1}{2i}[J(\mathbf{k}+\mathbf{Q}) - J(\mathbf{k}-\mathbf{Q})]\cos\theta,$$

where $J(\mathbf{k})$ is the Fourier transform of the interactions, given in Eq. (5). The canting angle $\theta$ is fixed by

$$\cos\theta = \frac{h}{J(0) - J(\mathbf{Q})}. \quad \text{(A34)}$$

Next we describe the LSW theory of the quantum spin-$S$ model. After the rotation to the local frames and a Holstein-Primakoff transformation of spin operators into bosonic creation and destruction operators $a_{\mathbf{k}}^\dagger$ and $a_{\mathbf{k}}$, the harmonic Hamiltonian for spin $S$ is written as [76,86]

$$\mathcal{H}_{qu}^{(2)} = \frac{1}{2} \sum_{\mathbf{k}} [\hat{\mathbf{a}}_{\mathbf{k}}^\dagger M(\mathbf{k}) \hat{\mathbf{a}}_{\mathbf{k}} - \Delta_{\mathbf{k}}], \quad \text{(A35)}$$

where

$$\hat{\mathbf{a}}_{\mathbf{k}}^\dagger = (a_{\mathbf{k}}^\dagger, a_{-\mathbf{k}}) \quad \text{(A36)}$$

and

$$\Delta_{\mathbf{k}} = -SJ(\mathbf{Q}) \quad \text{(A37)}$$

(cf. [87]). The $2 \times 2$ matrix $M(\mathbf{k})$ is given by

$$M(\mathbf{k}) = \begin{bmatrix} A(\mathbf{k}) + C(\mathbf{k}) & B(\mathbf{k}) \\ B(\mathbf{k}) & A(\mathbf{k}) - C(\mathbf{k}) \end{bmatrix}, \quad \text{(A38)}$$

with

$$A(\mathbf{k}) = \frac{S}{4}\{(\cos^2\theta + 1)[J(\mathbf{k}+\mathbf{Q}) + J(\mathbf{k}-\mathbf{Q})] - 4J(\mathbf{Q})$$

$$+ 2\sin^2\theta J(\mathbf{k})\},$$

$$B(\mathbf{k}) = \frac{S}{4}\sin^2\theta[J(\mathbf{k}+\mathbf{Q}) + J(\mathbf{k}-\mathbf{Q}) - 2J(\mathbf{k})],$$

$$C(\mathbf{k}) = \frac{S}{2}\cos\theta[J(\mathbf{k}+\mathbf{Q}) - J(\mathbf{k}-\mathbf{Q})]. \quad \text{(A39)}$$

A Bogoliubov transformation,

$$\hat{\mathbf{a}}_{\mathbf{k}} = T_{\mathbf{k}}\hat{\mathbf{b}}_{\mathbf{k}}, \tag{A40}$$

brings $\mathcal{H}_{\text{qu}}^{(2)}$ into a diagonal form,

$$\mathcal{H}_{\text{qu}}^{(2)} = \frac{1}{2}\sum_{\mathbf{k}}[\hat{\mathbf{b}}_{\mathbf{k}}^{\dagger}\Omega(\mathbf{k})\hat{\mathbf{b}}_{\mathbf{k}} - \Delta_{\mathbf{k}}], \tag{A41}$$

with

$$\Omega(\mathbf{k}) = \begin{bmatrix} \omega_{\mathbf{k}} & 0 \\ 0 & \omega_{-\mathbf{k}} \end{bmatrix}, \tag{A42}$$

where the spin-wave dispersion is

$$\omega_{\mathbf{k}} = \sqrt{[A(\mathbf{k}) + B(\mathbf{k})][A(\mathbf{k}) - B(\mathbf{k})]} + C(\mathbf{k}). \tag{A43}$$

In the case of $S = 1$ we have the following relations:

$$\begin{aligned} \mathcal{M}^{xx}(\mathbf{k}) &= A(\mathbf{k}) + B(\mathbf{k}), \\ \mathcal{M}^{yy}(\mathbf{k}) &= A(\mathbf{k}) - B(\mathbf{k}), \\ \mathcal{M}^{xy}(\mathbf{k}) &= iC(\mathbf{k}). \end{aligned} \tag{A44}$$

One can indeed directly see from Eqs. (A43) and (A44) that

$$\begin{aligned} \omega_{\mathbf{k}}\omega_{-\mathbf{k}} &= A^2(\mathbf{k}) - B^2(\mathbf{k}) - C^2(\mathbf{k}) \\ &= \mathcal{M}^{xx}(\mathbf{k})\mathcal{M}^{yy}(\mathbf{k}) - |\mathcal{M}^{xy}(\mathbf{k})|^2 \\ &= |\mathcal{M}(\mathbf{k})|, \end{aligned} \tag{A45}$$

and hence

$$\frac{S_{sw}}{N} = -\frac{1}{N}\sum_{\mathbf{k}}\ln\omega_{\mathbf{k}} = -\langle\ln\omega_{\mathbf{k}}\rangle. \tag{A46}$$

### 4. Spin-wave dispersion in coplanar $K$-sublattice states

We now turn to the case of coplanar ground states such as the $Y$ state with an in-plane field (or the coplanar $4Q$ state in zero field) which require the introduction of $K$ sublattices. For the sake of greater generality we rewrite the Hamiltonian as

$$\mathcal{H} = \sum_{\langle\nu,m;\nu',m'\rangle} J_{\nu,m;\nu',m'}\mathbf{S}_{\nu,m}\cdot\mathbf{S}_{\nu',m'} - \mathbf{h}\cdot\sum_{\nu,m}\mathbf{S}_{\nu,m}. \tag{A47}$$

The Fourier transform of the exchange couplings is defined by

$$J_{\nu,\nu'}(\mathbf{k}) = \sum_{m}J_{\nu,0;\nu',m}e^{i\mathbf{k}\cdot(\mathbf{R}_{\nu',m}-\mathbf{R}_{\nu,0})}. \tag{A48}$$

Choosing the reference frame such that the ground-state spins lie in the $S^x$-$S^z$ plane, with $\mathbf{h}$ along the $S^z$ axis, the ground-state spins can then be written as in Eq. (A1), with $\theta = \pi/2$ for all sites and $\phi_{\nu,m} = \phi_\nu$ independent of the unit cell. After expressing the spin deviations in the local frames, one obtains a harmonic Hamiltonian of the form Eq. (A4) with

$$\mathcal{M}(\mathbf{k}) = \begin{bmatrix} \mathcal{M}^{xx}(\mathbf{k}) & \mathcal{M}^{xy}(\mathbf{k}) \\ \mathcal{M}^{yx}(\mathbf{k}) & \mathcal{M}^{yy}(\mathbf{k}) \end{bmatrix}, \tag{A49}$$

where $\mathcal{M}^{\alpha\beta}(\mathbf{k})$ $(\alpha,\beta = x,y)$ are $K \times K$ matrices given by

$$\begin{aligned} \mathcal{M}_{\nu,\nu'}^{xx}(\mathbf{k}) &= J_{\nu,\nu'}(\mathbf{k})\cos\phi_{\nu,\nu'} + \delta_{\nu,\nu'}[h\cos\phi_\nu - N_\nu], \\ \mathcal{M}_{\nu,\nu'}^{yy}(\mathbf{k}) &= J_{\nu,\nu'}(\mathbf{k}) + \delta_{\nu,\nu'}[h\cos\phi_\nu - N_\nu], \\ \mathcal{M}_{\nu,\nu'}^{yy}(\mathbf{k}) &= \mathcal{M}^{yx}(\mathbf{k}) = 0, \end{aligned} \tag{A50}$$

with $\phi_{\nu,\nu'} = \phi_\nu - \phi_{\nu'}$ and

$$N_\nu = \sum_{\nu'}J_{\nu,\nu'}(0)\cos\phi_{\nu,\nu'}. \tag{A51}$$

There are $K = 3$ sublattices in the $Y$ state. The expressions for the angles $\phi_\nu$ are similar to those found for the triangular antiferromagnet,

$$\phi_1 = \pi,$$

$$\phi_2 = -\phi_3 = \arccos\frac{1}{2}\left(\frac{h}{3J_\triangle} + 1\right), \tag{A52}$$

where $J_\triangle$ is given in Eq. (13), whereas the exchange couplings Eq. (A48) are

$$\begin{aligned} J_{\nu,\nu}(\mathbf{k}) &= J_1\cos(k_y) + J_3\cos(2k_y), \quad \{\nu = 1,2,3\} \\ J_{1,2}(\mathbf{k}) &= J_{2,3}(\mathbf{k}) = J_{3,1}(\mathbf{k}) \\ &= \frac{J_1}{2}e^{ik_x} + J_2e^{ik_x}\cos(k_y) + \frac{J_3}{2}e^{-2ik_x}. \end{aligned} \tag{A53}$$

For the $4Q$ states the number of sublattices is $K = 10$ and we do not show the matrix of couplings $J_{\nu,\nu'}(\mathbf{k})$.

### 5. Spin-wave dispersion in canted $K$-sublattice states

Here we consider canted conical states with $K$ sublattices. As for the case of conical spirals, the reference frame is chosen such that the magnetic field is along the $S^y$ axis and the ground-state spins can then be written as in Eq. (A1). These canted conical states have equal projections of the spins along the field (equal values of $\theta$ for all sites), whereas the spin projections in the $S^x$-$S^z$ plane form a $K$ sublattice configuration and include, as a special case, the $4Q$ state where the spins uniformly cant in the direction of the magnetic field.

The ground state has equal $\theta$ for all sites and $\phi_{\nu,m} = \phi_\nu$ independent of the unit cell. The matrix $\mathcal{M}(\mathbf{k})$ has the same structure as in Eq. (A49) but with

$$\begin{aligned} \mathcal{M}_{\nu,\nu'}^{xx}(\mathbf{k}) &= J_{\nu,\nu'}(\mathbf{k})\cos\phi_{\nu,\nu'} - \delta_{\nu,\nu'}N_\nu, \\ \mathcal{M}_{\nu,\nu'}^{yy}(\mathbf{k}) &= \mathcal{M}_{\nu,\nu'}^{xx}(\mathbf{k})\cos^2\theta + [J_{\nu,\nu'}(\mathbf{k}) - \delta_{\nu,\nu'}N_\nu]\sin^2\theta, \\ \mathcal{M}_{\nu,\nu'}^{xy}(\mathbf{k}) &= [J_{\nu,\nu'}(\mathbf{k}) - J_{\nu,\nu'}(-\mathbf{k})]\sin\phi_{\nu,\nu'}\cos\theta, \end{aligned} \tag{A54}$$

where the canting angle $\theta$ is related to the applied field by

$$\cos\theta = \frac{hK}{\sum_{\nu\nu'}J_{\nu,\nu'}(0)(1 - \cos\phi_{\nu,\nu'})}. \tag{A55}$$

In the case of a commensurate spiral state, $\phi_\nu = \mathbf{Q}\cdot\mathbf{R}_{\nu,0}$, one can check that, as expected, $\mathcal{H}^{(2)}$ [Eq. (A4)] can be rewritten in the form Eq. (A32) with the coefficients Eq. (A33), where

$$J(\mathbf{k}) = \sum_\nu J_{1,\nu}(\mathbf{k})e^{i\mathbf{k}\cdot\mathbf{R}_{\nu,0}}. \tag{A56}$$

For the same reasons as above, Eq. (A31) holds and the entropy factor can be alternatively computed from the spin-wave frequencies.

### 6. Spin-wave dispersion in spiral states

In the main text we investigate the fingerprints of the spin waves of spiral states in the uniform paramagnetic phase. For this purpose, the spin-wave spectrum of the fully
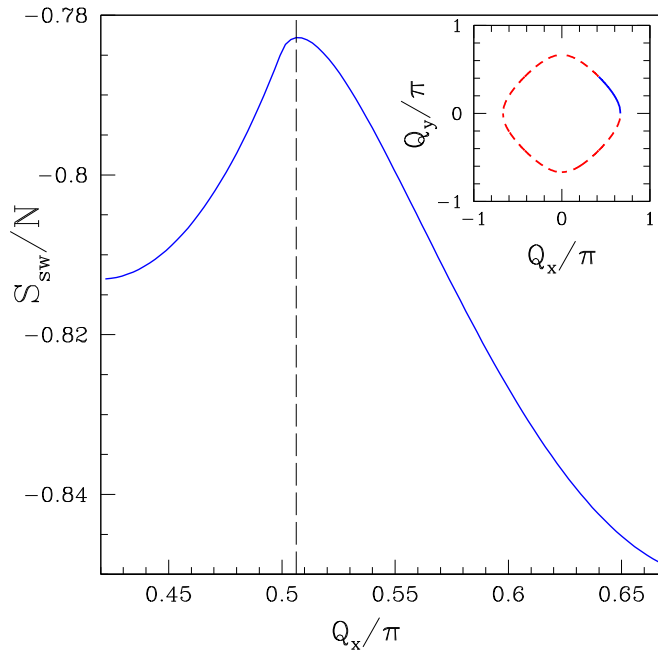
FIG. 15. Entropy per spin $S_{sw}/N$ of the two-dimensional spiral states which make up the classical ground state manifold of $\mathcal{H}_{\square}^{\text{FFM}}$ [cf. Eq (1)] for the parameter set $\mathbf{J}_B$ [Eq. (22)]. The inset shows the set of wave vectors associated with the ground-state manifold, as defined by Eq. (20). Thermal fluctuations select the state with highest entropy, which corresponds to a an incommensurate spiral with wave vector close to $(\pi/2,\pi/3)$. $S_{sw}/N$ was calculated through Eq. (A46), using the linear spin-wave dispersion $\omega(\mathbf{k})$ [Eq. (A43)], as discussed in Appendix A.



FIG. 16. Entropy per spin $S_{sw}/N$ [Eq. (A46)] of different competing states as a function of magnetic field $h$. The entropy of the coplanar $Y$ state increases with increasing field and, for $0.8J_\triangle < h < 3J_\triangle$, overtakes that of the conical state with $\mathbf{Q} = (\pi/2,\pi/3)$. Entropy was calculated with linear spin-wave (LSW) theory for the parameter set $\mathbf{J}_B$ [Eq. (22)], as discussed in Appendix A. Within this linear, low-temperature approximation, the $4Q$ state is not selected by fluctuations at any value of magnetic field.

polarized state provides useful information about the low-energy excitations above the ring. The dispersion relation is obtained at the saturation field in a straightforward manner as

$$\omega(\mathbf{k})_{1SL} = J(\mathbf{k}) - J(\mathbf{Q}), \qquad (A57)$$

which has the lowest energy at the spiral wave vector $\mathbf{Q}$. By imposing a low-energy cutoff, we can identify momenta close to the ring, which contribute to the low-energy excitations, and use them in Eq. (44) to calculate the total structure factor associated with the ring.

It would be interesting to see how this dispersion is modified in the spiral ordered phase. Here we consider the coplanar spiral state at zero field. The dispersion is obtained from Eq. (A43) by setting $S = 1$ and $\theta = \pi/2$,

$$\omega(\mathbf{k}) = \sqrt{\frac{1}{2}[J(\mathbf{k}+\mathbf{Q}) + J(\mathbf{k}-\mathbf{Q}) - 2J(\mathbf{Q})][J(\mathbf{k}) - J(\mathbf{Q})]}. \qquad (A58)$$

When $\mathbf{k}$ is close to the spiral wave vector $\mathbf{Q}$, one finds

$$\omega(\mathbf{k}) \approx \sqrt{\mathsf{J}[J(\mathbf{k}) - J(\mathbf{Q})]}, \qquad (A59)$$

where $\mathsf{J} = [J(2\mathbf{Q}) + J(0)]/2 - J(\mathbf{Q})$. At the parameter set $\mathbf{J}_B$, the spin-wave dispersion has gapless line modes along $\mathbf{k} = \mathbf{Q}^{\text{ring}}$ [Eq. (20)] in the LSW approximation.
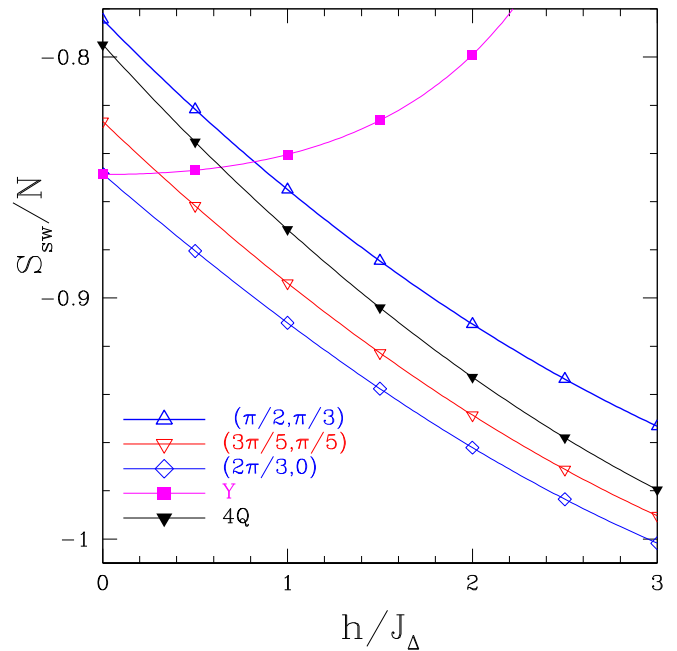
## APPENDIX B: ENTROPY SELECTION OF A SPIRAL WITH Q ≈ (π/2,π/3) OUT OF THE DEGENERATE RING IN THE HARMONIC APPROXIMATION

In this appendix we show how, for the parameter set $\mathbf{J}_B$ [Eq. (22)], the harmonic analysis developed in Appendix A predicts the entropic selection of a spiral state at low temperatures and vanishing magnetic field, as suggested by Monte Carlo simulations. In Fig. 15 we plot the the entropy per spin $S_{sw}/N$ [Eq. (A11)] for the the family of conical states with wave vector $\mathbf{Q} = (Q_x, Q_y)$ satisfying the ring equation Eq. (20), in the absence of an applied magnetic field. This was computed from the spin-wave frequencies [Eqs. (A46) and (A43)] and is $S_{sw}/N$ plotted as a function of $Q_x$.

Thermal fluctuations select, within the degenerate ring, the spiral state with the highest entropy, which is described by an incommensurate wave vector slightly away from $(\pi/2,\pi/3)$, or wave vectors related to it by symmetry. This result is supported by the Monte Carlo simulations [see Sec. (IV B)] and continues to hold for a small applied field, where the state evolves from a coplanar into a conical spiral.

## APPENDIX C: ENTROPY COMPETITION BETWEEN THE Q ≈ (π/2,π/3) 1Q CONE AND THE COPLANAR Y STATES IN THE HARMONIC APPROXIMATION

In this appendix we show how, for the parameter set $\mathbf{J}_B$ [Eq. (22)], a canted $Y$ state prevails over a conical version of the spiral state at low temperatures, for a sufficiently strong

applied magnetic field. In Fig. 16, we plot the entropy per spin $S_{sw}/N$ [Eq. (A11)] for a selection of different states within the degenerate ground-state manifold as a function of magnetic field, calculated using the results of Appendixes A 3 and A 5 . The entropy factor of the coplanar $Y$ state increases with increasing field, until it is finally selected by at low-temperature fluctuations for $0.8J_\triangle \lesssim h < 3J_\triangle$ as supported by the Monte Carlo simulations [see Sec. (IV B)]. The $4Q$ state is not favored by thermal fluctuations at low temperature, which is again in agreement with the simulation results. However, its entropy factor at low field is rather close to the one of the most favored conical spirals. This small difference is overcome by anharmonic effects which stabilize the $4Q$ state at larger $T$ for field $h \lesssim 0.8J_\triangle$.

## APPENDIX D: QUANTUM SELECTION OUT OF THE DEGENERATE RING IN THE QUANTUM MODEL IN THE LARGE-$S$ LIMIT.

In this appendix we discusses the role of quantum fluctuations in selecting an ordered ground state from the degenerate ground-state manifold for the parameter set $\mathbf{J}_B$ [Eq. (22)], within the linear spin-wave (LSW) theory developed in Appendix A 2. From the LSW expansion of the quantum model [Eq. (A19)], one finds that the ground-state energy per spin in the large-$S$ limit can be written as

$$e_{\mathrm{qu}} = e_0 + \Delta e, \tag{D1}$$

where $e_0$ is the ground-state energy per spin of the classical model and $\Delta e$ is its first-order correction in $1/S$ due to the the zero point motion of the spin waves,

$$\Delta e = \frac{1}{2N} \sum_{\mathbf{k}} [\mathrm{Tr}(\tilde{\omega}_{\mathbf{k}}) - \Delta_{\mathbf{k}}]. \tag{D2}$$

Here $\Delta e$ is proportional to $S$, whereas $e_0$ is proportional to $S^2$. Among a set of classically degenerate ground states, quantum fluctuations will favor the state which minimizes $\Delta e$.

For conical spirals,

$$e_0 = \frac{S^2}{2}[J(0)\cos^2\theta + J(\mathbf{Q})\sin^2\theta] + hS\cos\theta, \tag{D3}$$
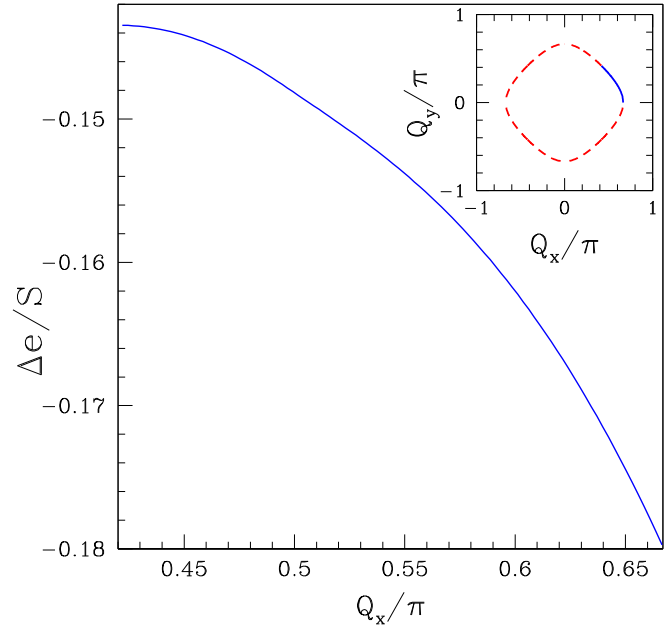


FIG. 17. Quantum correction $\Delta e/S$ to the ground-state energy (per spin) of spiral states [Eq. (D4)] for the spin-$S$ quantum model discussed in Appendix A 2. Calculations were carried out within the linear spin-wave theory (LSW), for coplanar spiral states with wave vector $\mathbf{Q}$ belonging to the classical ground-state manifold in the absence of magnetic field, for the parameter set $\mathbf{J}_B$ [Eq. (22)]. The inset shows the range of wave vectors considered. Quantum fluctuations select a spiral with $\mathbf{Q} = (2\pi/3, 0)$ and symmetry-related states.

which reduces to $e_0 = S^2 J(\mathbf{Q})/2$ in zero field, and

$$\Delta e = \frac{1}{2N}\sum_{\mathbf{k}} \omega_{\mathbf{k}} + \frac{S}{2}J(\mathbf{Q}). \tag{D4}$$

In Fig. 17 we show $\Delta e/S$ at the $\mathbf{J}_B$ point in zero field for the family of conical states with wave vector $\mathbf{Q} = (Q_x, Q_y)$ satisfying the ring equation Eq. (20). One sees that quantum fluctuations favor the three-sublattice stripe states with $\mathbf{Q} = (\pm 2\pi/3, 0)$ or $\mathbf{Q} = (0, \pm 2\pi/3)$.

A similar calculation based on the LSW theory for the $K$-sublattice cases [Eq. (A19)] shows that, in zero field, the $4Q$ state has a higher energy than the $\mathbf{Q} = (2\pi/3, 0)$ spiral state (or equivalently the $Y$ state at zero field). In a finite field, the $Y$ state becomes favored over the conical spirals and the canted $4Q$ state.

[1] L. Balents, Nature (London) **464**, 199 (2010).

[2] R. Moessner, J. Phys.: Conf. Ser. **145**, 012001 (2009).

[3] O. A. Starykh, Rep. Prog. Phys. **78**, 052502 (2015).

[4] H. Matsuda and T. Tsuneto, Prog. Theor. Phys. Suppl. **46**, 411 (1970).

[5] K. S. Liu and M. E. Fisher, J. Low Temp. Phys. **10**, 655 (1973).

[6] H. Kawamura and S. Miyashita, J. Phys. Soc. Jpn. **54**, 4530 (1985).

[7] L. Seabra and N. Shannon, Phys. Rev. Lett. **104**, 237205 (2010).

[8] A. Andreev and I. Grishchuk, JETP **87**, 467 (1984).

[9] N. Shannon, T. Momoi, and P. Sindzingre, Phys. Rev. Lett. **96**, 027213 (2006).

[10] A. Smerald and N. Shannon, Phys. Rev. B **88**, 184430 (2013).

[11] S. Mühlbauer, B. Binz, F. Jonietz, C. Pfleiderer, A. Rosch, A. Neubauer, R. Georgii, and P. Böni, Science **323**, 915 (2009).

[12] T. Schulz, R. Ritz, A. Bauer, M. Halder, M. Wagner, C. Franz, C. Pfleiderer, K. Everschor, M. Garst, and A. Rosch, Nat. Phys. **8**, 301 (2012).

[13] C. Castelnovo, R. Moessner, and S. L. Sondhi, Annu. Rev. Condens. Matter Phys. **3**, 35 (2012).

[14] T. Momoi, P. Sindzingre, and K. Kubo, Phys. Rev. Lett. **108**, 057206 (2012).

[15] A. Casey, M. Neumann, B. Cowan, J. Saunders, and N. Shannon, Phys. Rev. Lett. **111**, 125302 (2013).

[16] E. E. Kaul, H. Rosner, N. Shannon, R. V. Shpanchenko, and C. Geibel, J. Magn. Magn. Mater. **272-276**, 922 (2004).

[17] R. Nath, A. A. Tsirlin, H. Rosner, and C. Geibel, Phys. Rev. B **78**, 064422 (2008).

[18] M. Skoulatos, J. P. Goff, C. Geibel, E. E. Kaul, R. Nath, N. Shannon, B. Schmidt, A. P. Murani, P. P. Deen, M. Enderle, and A. R. Wildes, Europhys. Lett. **88**, 57005 (2009).

[19] H. Kageyama, T. Kitano, N. Oba, M. Nishi, S. Nagai, K. Hirota, L. Viciu, J. B. Wiley, J. Yasuda, Y. Baba, Y. Ajiro, and K. Yoshimura, J. Phys. Soc. Jpn. **74**, 1702 (2005).

[20] Y. Tsujimoto, Y. Baba, N. Oba, H. Kageyama, T. Fukui, Y. Narumi, K. Kindo, T. Saito, M. Takano, Y. Ajiro, and K. Yoshimura, J. Phys. Soc. Jpn. **76**, 063711 (2007).

[21] S. M. Yusuf, A. K. Bera, C. Ritter, Y. Tsujimoto, Y. Ajiro, H. Kageyama, and J. P. Attfield, Phys. Rev. B **84**, 064407 (2011).

[22] C. Tassel *et al.*, Phys. Rev. Lett. **105**, 167205 (2010).

[23] L. Seabra, T. Momoi, P. Sindzingre, and N. Shannon, Phys. Rev. B **84**, 214418 (2011).

[24] G. Misguich and C. Lhuillier, *Frustrated Spin Systems*, 2nd ed., edited by H. T. Diep (World Scientific, Singapore, 2004).

[25] H.-C. Jiang, H. Yao, and L. Balents, Phys. Rev. B **86**, 024424 (2012).

[26] R. L. Doretto, Phys. Rev. B **89**, 104415 (2014).

[27] Shou-Shu Gong, W. Zhu, D. N. Sheng, O. I. Motrunich, and M. P. A. Fisher, Phys. Rev. Lett. **113**, 027201 (2014).

[28] W. J. Hu, F. Becca, A. Parola, and S. Sorella, Phys. Rev. B **88**, 060402(R) (2013).

[29] Q. Si and E. Abrahams, Phys. Rev. Lett. **101**, 076401 (2008).

[30] A. Smerald and N. Shannon, Europhys. Lett. **92**, 47005 (2010).

[31] P. C. Dai, Rev. Mod. Phys. **87**, 855 (2015).

[32] N. Shannon, B. Schmidt, K. Penc, and P. Thalmeier, Eur. Phys. J. B **38**, 599 (2004).

[33] R. Shindou, S. Yunoki, and T. Momoi, Phys. Rev. B **84**, 134414 (2011).

[34] J. Richter, R. Darradi, J. Schulenburg, D. J. J. Farnell, and H. Rosner, Phys. Rev. B **81**, 174429 (2010).

[35] A. Smerald, H. T. Ueda, and N. Shannon, Phys. Rev. B **91**, 174402 (2015).

[36] M. E. Zhitomirsky and H. Tsunetsugu, Europhys. Lett. **92**, 37001 (2010).

[37] B. Schmidt, P. Thalmeier, and N. Shannon, Phys. Rev. B **76**, 125113 (2007).

[38] P. Thalmeier, M. E. Zhitomirsky, B. Schmidt, and N. Shannon, Phys. Rev. B **77**, 104441 (2008).

[39] A. A. Tsirlin, B. Schmidt, Y. Skourski, R. Nath, C. Geibel, and H. Rosner, Phys. Rev. B **80**, 132407 (2009).

[40] H. T. Ueda and K. Totsuka, Phys. Rev. B **80**, 014417 (2009).

[41] E. Rastelli, L. Reatto, and A. Tassi, J. Phys. C **18**, 353 (1985).

[42] H. T. Diep, Phys. Rev. B **39**, 397 (1989).

[43] E. Rastelli, L. Tassi, and L. Reatto, Physica B+C (Amsterdam) **97**, 1 (1979).

[44] E. Rastelli, L. Reatto, and A. Tassi, J. Phys. C **19**, 6623 (1986).

[45] A. V. Chubukov, J. Phys. C **17**, L991 (1984).

[46] P. Sindzingre, L. Seabra, N. Shannon, and T. Momoi, J. Phys.: Conf. Ser. **145**, 012048 (2009).

[47] P. Sindzingre, N. Shannon, and T. Momoi, J. Phys.: Conf. Ser. **200**, 022058 (2010).

[48] S. Okumura, H. Kawamura, T. Okubo, and Y. Motome, J. Phys. Soc. Jpn. **79**, 114705 (2010).

[49] H. D. Rosales, D. C. Cabra, C. A. Lamas, P. Pujol, and M. E. Zhitomirsky, Phys. Rev. B **87**, 104402 (2013).

[50] T. Okubo, T. H. Nguyen, and H. Kawamura, Phys. Rev. B **84**, 144432 (2011).

[51] T. Okubo, S. Chung, and H. Kawamura, Phys. Rev. Lett. **108**, 017206 (2012).

[52] Y. Kamiya and C. D. Batista, Phys. Rev. X **4**, 011023 (2014).

[53] H. D. Rosales, D. C. Cabra. and P. Pujol, Phys. Rev. B **92**, 214439 (2015).

[54] P. G. de Gennes, *Superconductivity of Metals and Alloys*, Advanced Books Classics (Westview Press, Boulder, CO, 1999).

[55] G. Blatter, M. V. Feigel'man, V. B. Geshkenbein, A. I. Larkin, and V. M. Vinokur, Rev. Mod. Phys. **66**, 1125 (1994).

[56] P. W. Anderson, Mater. Res. Bull. **8**, 153 (1973).

[57] R. Chen, H. Ju, H.-C. Jiang, O. A. Starykh, and L. Balents, Phys. Rev. B **87**, 165123 (2013).

[58] M. V. Gvozdikova, P.-E. Melchy, and M. E. Zhitomirsky, J. Phys. Condens. Matter **23**, 164209 (2011).

[59] C. L. Henley, Phys. Rev. Lett. **62**, 2056 (1989).

[60] A. V. Chubukov and D. I. Golosov, J. Phys. Condens. Matter **3**, 69 (1991).

[61] K. Hukushima and K. Nemoto, J. Phys. Soc. Jpn. **65**, 1604 (1996).

[62] L. Seabra and N. Shannon, Phys. Rev. B **83**, 134412 (2011).

[63] S. Miyashita and H. Shiba, J. Phys. Soc. Jpn. **53**, 1145 (1984).

[64] H. Kawamura, A. Yamamoto, and T. Okubo, J. Phys. Soc. Jpn. **79**, 023701 (2010).

[65] B. W. Southern and H-J. Xu, Phys. Rev. B **52**, R3836 (1995).

[66] B. Delamotte, M. Dudka, Yu. Holovatch, and D. Mouhanna, Phys. Rev. B **82**, 104432 (2010).

[67] N. Hasselmann and A. Sinner, Phys. Rev. B **90**, 094404 (2014).

[68] R. J. Baxter, J. Phys. C **6**, L445 (1973).

[69] R. J. Baxter, H. N. V. Temperley, and S. E. Ashley, Proc. R. Soc. London, Ser. A **358**, 535 (1978).

[70] D. R. Nelson and J. M. Kosterlitz, Phys. Rev. Lett. **39**, 1201 (1977).

[71] H. Weber and P. Minnhagen, Phys. Rev. B **37**, 5986 (1988).

[72] M. Y. Veillette, J. T. Chalker, and R. Coldea, Phys. Rev. B **71**, 214426 (2005).

[73] Jason Alicea, Andrey V. Chubukov, and Oleg A. Starykh, Phys. Rev. Lett. **102**, 137201 (2009).

[74] Luis Seabra (unpublished).

[75] M. E. Zhitomirsky, A. Honecker, and O. A. Petrenko, Phys. Rev. Lett. **85**, 3269 (2000).

[76] Tommaso Coletta, M. E. Zhitomirsky, and Frédéric Mila, Phys. Rev. B **87**, 060407(R) (2013).

[77] W. M. Saslow, M. Gabay, and W.-M. Zhang, Phys. Rev. Lett. **68**, 3627 (1992).

[78] A. B. Harris, E. Rastelli, and A. Tassi, Phys. Rev. B **44**, 2624 (1991).

[79] C. Henley, Annu. Rev. Condens. Matter Phys. **1**, 179 (2010).

[80] R. Moessner and J. T. Chalker, Phys. Rev. Lett. **80**, 2929 (1998).

[81] D. Bergman, J. Alicea, E. Gull, S. Trebst, and L. Balents, Nat. Phys. **3**, 487 (2007).

[82] E. Rastelli, L. Reatto, and A. Tassi, J. Phys. C **16**, L331 (1983).

[83] C. Schütte and A. Rosch, Phys. Rev. B **90**, 174432 (2014).

[84] The entropy per site is $\frac{S_{sw}}{N} + \ln T$, which is the average of the logarithm of a dimensionless ratio.

[85] J. H. P. Colpa, Physica A **93**, 327 (1978).

[86] Our expression of $B(\mathbf{k})$ in Eq. (A39) has opposite sign as we choose the spiral to cant toward the $y$ axis.

[87] One may check that $\sum_{\mathbf{k}} A(\mathbf{k}) - C(\mathbf{k}) = \sum_{\mathbf{k}} \Delta_{\mathbf{k}}$.